Hydrodynamic and sediment transport modelling in the Pearl River Estuary and adjacent Chinese coastal zone during Typhoon Mangkhut

Yun Yang[a,b], Weibing Guan[a,b,c,d*], Eric Deleersnijder[e], Zhiguo He[a]

[a] Ocean College, Zhejiang University, Zhoushan, 316021, China

[b] State Key Laboratory of Satellite Ocean Environment Dynamics, Second Institute of Oceanography, Ministry of Natural Resources, Hangzhou, 310012, China

[c] Southern Marine Science and Engineering Guangdong Laboratory (Zhuhai), Zhuhai, 519080, China

[d] School of Oceanography, Shanghai Jiao Tong University, Shanghai, 200030, China

[e] Institute of Mechanics, Materials and Civil Engineering (IMMC) & Earth and Life Institute (ELI), Université Catholique de Louvain, Avenue Georges Lemaître 4, 1348 Louvain-la-Neuve, Belgium

[*] Corresponding author: gwb@sio.org.cn

Abstract

Typhoon Mangkhut, in 2018, was one of the worst typhoons in recent history that has made landfall in the Pearl River Estuary (PRE) China. It swept along the coast of Guangdong Province, causing severe damage to many areas and affecting more than one million people. To study the hydrodynamics and sediment dynamics in different sub-regions of the PRE during the typhoon, we implemented a 3D wave-current-sediment coupled ocean model based on the Semi-implicit Cross-scale Hydroscience Integrated System Model (SCHISM). A series of numerical experiments were conducted to study the variation in suspended sediment concentration (SSC) under different external forcing mechanisms, including tides, waves, river discharges and strong winds. Moderate Resolution Imaging Spectroradiometer (MODIS) images, collected after the typhoon landed, were used to assess the simulation results. We found that in the area where the water depth was shallower than 20 m, the increased total suspended sediment concentration was dominated by the regional erosion of fine sediment which was caused by near-bottom wave orbital velocity and bottom shear stress, especially at the four western outlets and along the western coast of the PRE. For the deeper coastal zone, at depths between 20 and 30 m offshore of the western coast, the high total SSC resulted from the contribution of fine sediment transported from the upper and middle estuaries by southwestward advection. A small amount of sand eroded and migrated locally, owing to the corresponding increase in the bottom shear stress. The variation in SSC during the typhoon had a time lag compared with other dynamic conditions, resulting in a maximum 1 h delayed response after the typhoon made landfall. Based on the results of the sensitivity experiments under the same typhoon conditions, we found that, as a result of wave-enhanced bottom shear stress, the SSC values associated with wave-current interaction were significantly higher, by as much as 1.5 and 1.3 times those of simulations without the waves at the surface and near-bottom layers, respectively. This indicated that the sediment resuspension induced by waves was important during typhoon landfall. However, the strong wind-induced current was weakened owing to the joint effect of wave radiation stress and enhanced bottom stress; thus, considering wave effects, the magnitude of the resulting sediment transport rate was smaller than that without considering wave effects, especially in shallow waters. During the approach, landfall and retreat of Typhoon Mangkhut, Lingding Bay experienced two transitions from a slight state of sediment loss to a relatively high state of sediment gain, followed by an even greater state of sediment loss. During an M_2 tidal cycle after Typhoon Mangkhut made landfall, the net seaward suspended load sediment transport in Lingding Bay reached 0.37 megatonnes. For the typhoon period covering three

M_2 tidal cycles, the overall state of suspended load sediment transport in Lingding Bay was sediment loss, with the magnitude of sediment loss on the west side being larger than that of sediment gain on the east side. The magnitude of the overall sediment loss in Lingding Bay would be enlarged unrealistically by approximately 73% if the wave effects were excluded. In each period, the extent of sediment transport between the two sides of the bay was strengthened by the wave-current interaction under typhoon conditions. We determined that the net effect of wave-current interaction and strong wind-induced currents under typhoon conditions was a key factor for erosion, which resulted in SSC-influenced areas being approximately 8.7 and 4.4 times as large as those under normal weather conditions for the surface and near-bottom layers, respectively. The turbidity maximum moved from the West Shoal of Lingding Bay under normal weather to the Modaomen Estuary, which was the most affected area during the typhoon when wave effects were considered. We also showed that the relative location of the typhoon path with respect to the estuary had a more significant effect on erosion than the intensity of the typhoon.

Keywords: Sediment transport, Typhoon, Pearl River Estuary, SCHISM, Numerical modelling

1. Introduction

The Pearl River in Guangdong Province, China, is a general name for the river system that is fed by the Xijiang, Dongjiang, Beijiang and other smaller rivers. It is the second largest river in China in terms of flow rate and the third longest river in China, with a total length of 2,124 km and a total drainage area of 450,000 km^2. The Pearl River Estuary (PRE; Fig. 1; see Section 2.4 for details) over the northern shelf of the South China Sea (SCS) is funnel-shaped. The mean annual loads of freshwater and riverine sediments in recent years (2001–2017) were approximately 2.86×10^{11} m^3 and 30.4 Mt (megatonnes), respectively (Dai et al., 2008; Zhang et al., 2019). The water depth in the PRE is less than 5 m, except for two channels with depths of 5–15 m (Liu and Cai, 2019). Formed by the accumulation of sediments from the Pearl River, the Pearl River Delta is the largest plain in Guangdong and is one of the most developed and urbanised areas in China. Due to the demand for rapid economic development and improved implementation standards for offshore engineering projects, further study of the hydrodynamics and sedimentation in this area is needed.

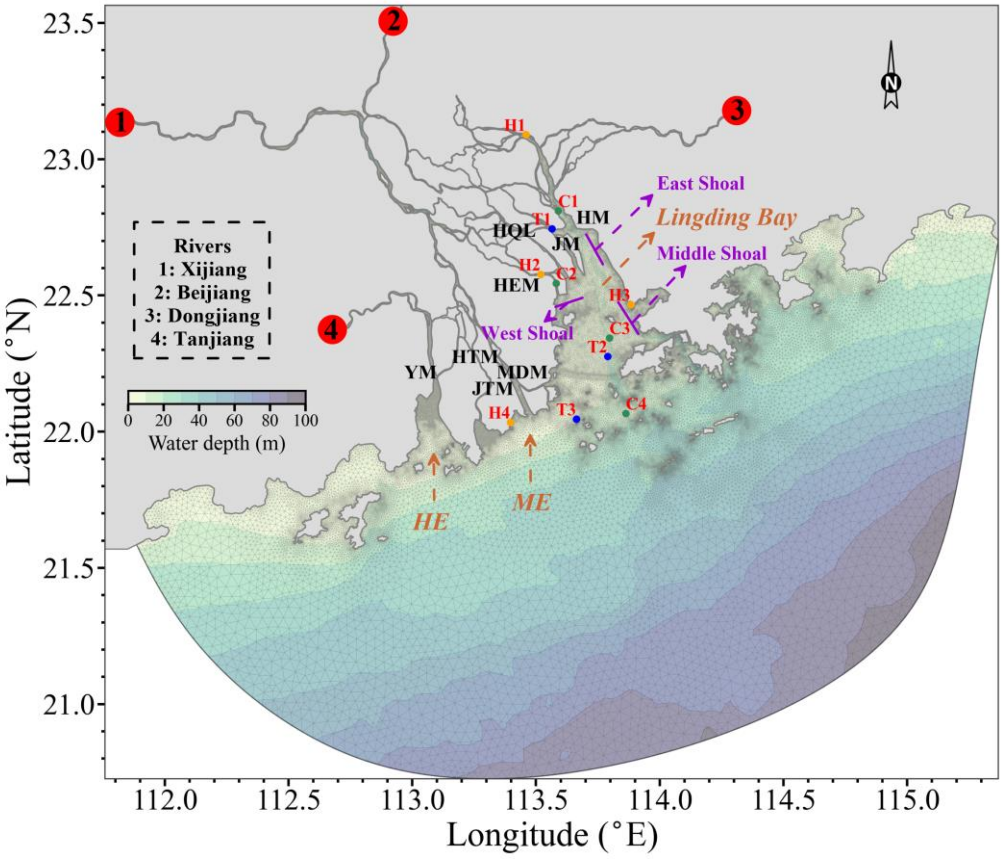

Fig. 1 Model mesh, water depth, observational stations (dots), and open boundaries. Blue dots: tide; green dots: current, salinity, and SSC; orange dots: storm surge. Eight outlets: Humen (**HM**), Jiaomen (**JM**), Hongqili (**HQL**), Hengmen (**HEM**), Modaomen (**MDM**), Jitimen (**JTM**), Hutiaomen (**HTM**), and Yamen (**YM**). ***HE*** is the Huangmaohai Estuary, and ***ME*** is the Modaomen Estuary.

The PRE is a terrigenous-saline-induced estuary with weak tides and high sediment loads (Shen et al., 2001). Researchers have focused on its hydrodynamic characteristics, sediment distribution and transport, particularly on the formation mechanism and seasonal changes in the turbidity maximum (TM). Previous studies on hydrodynamic mechanisms focused mainly on the variation of tidal energy flux and tidal dissipation, the diffusion route of diluted water, the salinity front, river plume and upwelling in the PRE during different seasons (Wong et al., 2003; Wong et al., 2004; Pang et al., 2006; Gan et al., 2009; Ni et al., 2011; Zhang et al., 2011). Early research and analysis based on field surveys found that the primary mechanisms for TM formation in the PRE are gravitational circulation, tidal trapping, sediment resuspension and deposition processes (Tian, 1986; Wai et al., 2004). In view of the unique topography and hydrodynamic conditions of the PRE, a few two-dimensional (2D; Zhang et al., 2000; Wang et al, 2001) and three-dimensional (3D; Chen et al, 1999; Chen et al., 2003; Guan et al., 2003; Hu et al., 2011) sediment transport models have been developed. These modelling studies generally focused on model validation and sediment distribution. A 3D hydrodynamic and sediment transport model revealed that the TM location in the PRE is highly consistent with the locations of the stagnation point, saltwater wedge and sand barriers (Wang and Wai, 2006). Both the total discharge and suspended sediment load of the Pearl River show significant seasonal variations. Approximately 80% of the river discharge and 95% of the sediment load are delivered during the wet season from April to September (Dong et al., 2006). In the same period, the inner Lingding Bay and Modaomen outlet (one

of the eight outlets in the PRE) have the largest deposits, and sediments are rapidly deposited around the West Shoal (WS) and Modaomen outlet (Hu and Li, 2009). The mechanism of the TM zone is different between the Middle Shoal and the WS. Both resuspension and sedimentation processes have significant impacts on the TM zone of the Middle Shoal, while gravitational circulation is crucial to the formation of the TM zone in the WS (Zhu et al., 2013). During the dry season, the suspended sediment concentration (SSC) is enhanced and the TM is intensified (Liu et al., 2016). The Coupled Ocean Atmosphere Wave Sediment Transport (COAWST) modelling system was used to study multi-sourced sediment transport in the PRE during a typical wet season in 2007 (Zhang et al., 2019). This illustrates that seaward sediment transport in the upper estuary is dominated by river discharge and tidal forcing in the lower channels, and that sediment transport in the lower shoals is controlled by tides and wind.

Guangdong Province is one of the provinces in China most affected by tropical cyclones (TCs). From 1949 to 2001, 205 TCs landed in Guangdong (Wang et al., 2003). According to the historical TC tracks, the PRE is the area where typhoons frequently made landfall, with a relative concentration from July to September which is consistent with the region's flood season. Powerful typhoon surges and storm-induced currents can easily cause the siltation of a large amount of sediment in nearshore shallow waters over a short period of time and even cause serious damage to offshore engineering structures, such as dikes and breakwaters. Moreover, wave-current interactions can strongly impact storm surges, estuarine currents and material transport during storms, according to a study conducted during Typhoon Hato using COAWST modelling (Chen et al., 2019).

Worldwide, research on the mechanism of sediment transport during storms has been undertaken since the 1980s (Cacchione and Drake, 1982). In the early years, researchers collected field data to analyse and understand sediment movement under the action of storms, which provided an important reference for physical model experiments and numerical simulations (Green et al., 1995; Morton et al., 1995; Williams and Rose, 2001). Subsequently, 2D (Zhang et al., 1999) and 3D models were established to simulate sediment transport during storms, mainly focusing on the parameters of sediment dynamics. Two idealised simulations were carried out using the Regional Ocean Modelling System (ROMS) coupled with the Simulating Waves Nearshore (SWAN) model to explore the effects of northeasters on the transport and fate of sediments in Massachusetts Bay (Warner et al., 2008). The important role of storm wind in driving suspended sediments in Apalachicola Bay was shown by a 3D coupled hydrodynamic, sediment transport and water quality model which also contributed to the understanding of the ecology of the region (Liu and Huang, 2009). In idealised cases, the Delft3D numerical model demonstrated that sediment transport at different locations within the Rhone mouth in the Mediterranean Sea was influenced by different dominant factors, including river flow, an equilibrium between the influence of floods and storms and the succession of these events (Boudet et al., 2017).

In China, coupled numerical modelling studies of sediment transport during storms have been carried out for various estuaries and bays, with an emphasis on sudden siltation caused by the joint action of hydrodynamic conditions, sediment sources and sedimentary environments under the action of storm surges (Ding et al., 2003; Yang et al., 2005; Zhao, 2007). Typhoon Mangkhut was the strongest typhoon that landed in China in 2018 (Liu et al., 2019), affecting ~4.65 million people and causing a direct economic loss of 13.68 billion Renminbi. It would be useful to collect data during such events on parameters such as currents, waves and sediment transport. However, it is too risky to collect data from coastal regions during the approach of a typhoon. Moreover, satellite remote sensing images of typhoon-affected areas are often of little use owing to typhoon clouds. Therefore, we set up a 3D

typhoon-wave-sediment coupled model to study sediment dynamics and predict the suspended sediment transport in the PRE during Typhoon Mangkhut. We also validated our model results using observations. The results of the coupled model show the feasibility of representing suspended sediment distribution and transport via comparison with remote sensing data on the days shortly after the typhoon landed. The consistency of the simulated results from the coupled model and the remote sensing data gathered after the typhoon shows that the model results are useful for analysing suspended sediment distribution and transport.

The model configuration and validation methods of the coupled model are described in Sections 2 and 3, respectively. The numerical results are presented in Section 4. In Section 5, sensitivity experiments are used to gain insights into the key factors affecting sediment transport during typhoons. Finally, the conclusions are presented in Section 6.

2. Coupled numerical model

2.1. Hydrodynamic model

The Semi-implicit Cross-scale Hydroscience Integrated System Model (SCHISM) is a 3D baroclinic finite element model that solves the primitive shallow-water equations on unstructured horizontal and vertical grids (Zhang et al., 2015, 2016). It is based on the SELFE v3.1dc model (Zhang and Baptista, 2008). The new enhancements and upgrades on the model include the following: (1) a new higher-order implicit advection scheme for transport (TVD^2); (2) a new advection scheme for the momentum equation (optional higher-order kriging with explicit, locally adaptive dissipation filter); (3) a new horizontal viscosity scheme (including bi-harmonic viscosity) to effectively filter out spurious inertial modes without introducing excessive dissipation; (4) a new vertical grid system (LSC^2; Zhang et al. 2015),; and (5) mixed triangular-quadrangular horizontal grid. The improved software is now distributed with an open-source Apache v2 licence. It uses a highly efficient and accurate semi-implicit finite element and finite volume method with an Eulerian-Lagrangian algorithm to solve the Navier-Stokes equations (in hydrostatic form) to address a wide range of physical and biological processes.

In this study, the hydrodynamic model at the core of SCHISM was used under the hydrostatic assumption and the Boussinesq approximation in Cartesian coordinates. The continuity equation in 3D form is:

$$\nabla \cdot \vec{u} + \frac{\partial w}{\partial z} = 0 \tag{1}$$

The horizontal momentum equation is:

$$\frac{D\vec{u}}{Dt} = \vec{F} - g\nabla\eta + \frac{\partial}{\partial z}\left(\nu \frac{\partial \vec{u}}{\partial z}\right) \tag{2}$$

The transport equation is:

$$\frac{DC}{Dt} = \frac{\partial}{\partial z}\left(\kappa \frac{\partial C}{\partial z}\right) + F_h + Q \tag{3}$$

Finally, the equation of state is:

$$\rho_w = \rho(S, T, p) \tag{4}$$

In the equations above, (x, y) are the horizontal coordinates, z is the vertical coordinate increasing upward, $\nabla = \left(\frac{\partial}{\partial x}, \frac{\partial}{\partial y}\right)$ is the horizontal gradient operator, and $\frac{D}{Dt}$ denotes material derivative. $\vec{u}$ is the horizontal velocity with Cartesian components (u, v), and w is the vertical velocity; t is the time, g is the gravitational acceleration, η is the free surface elevation, ν is the vertical eddy viscosity, C is the tracer concentration, κ is the vertical eddy diffusivity for tracers, F_h represents horizontal diffusion, h is bathymetric depth and Q is the mass source/sink. ρ_w is the water density which depends on the salinity, temperature and hydrostatic pressure. $\vec{F}$ in Eq. (2) represents the other forcing terms for momentum, including the horizontal viscosity term, Coriolis force, atmospheric pressure force, Earth tidal potential, baroclinic gradient and radiation stress, which are given as follows:

$$\vec{F} = \nabla \cdot (\mu \nabla \vec{u}) - f\vec{k} \times \vec{u} - \frac{1}{\rho_0}\nabla p_A + \alpha g \nabla \varphi - \frac{g}{\rho_0}\int_z^\eta \nabla \rho_w d\zeta + \overrightarrow{R_s} \tag{5}$$

where μ is the horizontal eddy viscosity; $\vec{k}$ is a unit vector for the z-axis (pointing vertically upward); f is the Coriolis parameter; ρ_0 is the reference water density; p_A is the atmospheric pressure; α is the effective Earth-elasticity factor; and φ is the Earth's tidal potential. When wave-induced stresses are considered in the model experiment, the radiation stress $\overrightarrow{R_s}$ is an additional term, treated explicitly, which will be detailed in Section 2.2.

The generic length-scale (GLS) model of Umlauf and Burchard (2003) was used to evaluate the eddy coefficients. It has the advantage of encompassing most of the two-equation closure schemes.

2.2. Wind wave model

Wind Wave Model III (WWMIII) is one of the first third-generation spectral wave models that solves the Eulerian form of the wave action equation (WAE) on unstructured meshes, incorporating most existing source terms for wind input and dissipation. WWMIII is based on the source code of Hsu et al. (2005). It was further developed by Roland and colleagues (Roland, 2009; Roland et al., 2012) in terms of numerical schemes and physics. The WAE solved by WWMIII can be expressed in Cartesian coordinates as follows:

$$\frac{\partial}{\partial t}N + \nabla_{\boldsymbol{X}}\left(\dot{\boldsymbol{X}}N\right) + \frac{\partial}{\partial \sigma}\left(\dot{\theta}N\right) + \frac{\partial}{\partial \theta}(\dot{\sigma}N) = S_{tot} \tag{6}$$

where N is the wave action density spectrum; $\boldsymbol{X}$ is the Cartesian coordinate vector (x, y) and $\dot{\boldsymbol{X}}$ is the advection velocity in the geographical space; σ is the relative wave frequency; θ is the wave direction; and $\dot{\theta}$ and $\dot{\sigma}$ are advection velocities in the spectral space. The term S_{tot} on the right-hand side is the net source, which is a function that includes the energy input due to wind (S_{in}), the nonlinear interaction in deep and shallow waters (S_{nl4} and S_{nl3}), the energy dissipation due to whitecapping and wave-breaking (S_{ds} and S_{br}) and the energy dissipation due to bottom friction (S_{bf}).

The radiation stress term $\overrightarrow{R_s}$ incorporated into $\vec{F}$ in Eq. (5), known as the net momentum of flux produced by wave transformation in shallow-water areas, simply adopts the formulation originally proposed by Longuet-Higgins and Stewart (1964), where the linear form in the horizontal plane is as follows:

$$\begin{cases} \overrightarrow{R_s} = (R_{sx}, R_{sy}) \\ R_{sx} = -\dfrac{1}{\rho_0(h+\eta)}\dfrac{\partial S_{xx}}{\partial x} - \dfrac{1}{\rho_0(h+\eta)}\dfrac{\partial S_{xy}}{\partial y} \\ R_{sy} = -\dfrac{1}{\rho_0(h+\eta)}\dfrac{\partial S_{yy}}{\partial y} - \dfrac{1}{\rho_0(h+\eta)}\dfrac{\partial S_{xy}}{\partial x} \end{cases} \quad (7)$$

In Eq. (7), S_{xx}, S_{xy}, and S_{yy} are the components of the radiation stress tensor, defined for a wave spectrum, according to Battjes (1974). Note that the stress is uniform in the vertical dimension under the above formulations (Roland et al., 2012).

From these formulations, the realisation of the two-way (wind waves and circulation) coupled model can be summarised as follows: the wave action *N* is computed from Eq. (6), which uses the source term S_{tot}; the components of the radiation stress tensor are computed using the wave action; these components are then passed on to Eq. (7) to calculate $\overrightarrow{R_s}$; the latter is included in $\vec{F}$ (see Eq. (5)), which is used in Eq. (2).

2.3. Sediment transport model

The SSC model used here is 3D (hereafter referred to as SED) which was incorporated using the hydrodynamic model as a passive tracer under the same spatial and temporal resolution. SSCs are computed by solving the advection-diffusion equation with an additional term for vertical settling, as follows:

$$\frac{\partial C_i}{\partial t} + \frac{\partial (uC_i)}{\partial x} + \frac{\partial (vC_i)}{\partial y} + \frac{\partial [(w - w_{s,i})C_i]}{\partial z} = \frac{\partial}{\partial z}\left(\kappa \frac{\partial C_i}{\partial z}\right) + F_h \quad (8)$$

$$w_{s,i}C_i + \kappa \frac{\partial C_i}{\partial z} = 0 \text{ at } z = \eta \quad (9)$$

$$w_{s,i}C_i + \kappa \frac{\partial C_i}{\partial z} = D_i - E_i \text{ at } z = -h \quad (10)$$

where C_i is the SSC of class *i* (kg m^{-3}), and $w_{s,i}$ is the sediment settling velocity of class *i* (m s^{-1}). For each sediment class *i*, the sediment settling velocity can be determined according to realistic conditions or, following Soulsby (1997):

$$w_{s,i} = \frac{\nu}{d_{50,i}}\left[\left(10.36^2 + 1.049{d_{*,i}}^3\right)^{0.5} - 10.36\right] \quad (11)$$

where $d_{50,i}$ is the median grain sediment diameter of class *i* (m) and $d_{*,i}$ is the dimensionless sediment diameter of class *i*, given by:

$$d_{*,i} = \left[\frac{g(s-1)}{\nu^2}\right]^{\frac{1}{3}} d_{50,i} \quad (12)$$

where $s = \frac{\rho_{s,i}}{\rho_w}$ is specific density and $\rho_{s,i}$ is the sediment density of class *i*.

The equation of state used to calculate seawater density from temperature and salinity is extended to include suspended sediment density effects as follows:

$$\rho = \rho_w + \sum_{i=1}^{Nsed} \frac{C_i}{\rho_{s,i}} \left(\rho_{s,i} - \rho_w\right) \tag{13}$$

where ρ is the local density (including salinity, temperature, and sediment effects) of the fluid (kg m^{-3}), and $Nsed$ is the total number of sediment classes.

The exchange of sediment between the flow and seabed is modelled using sink and source terms acting on the bottom computational cell. These terms model the quantity of sediment dropping out of the flow due to depositional flux (D_i in Eq. (10)) and the quantity of sediment entering the flow owing to the erosion flux (E_i in Eq. (10)). There is no net transport across the free surface; therefore, the diffusion flux is always balanced by the settling flux (Eq. (9)). At the sediment bed, the net sediment flux is equal to the sum of the sediment erosion flux and sediment deposition flux (Eq. (10)). For each sediment class *i*, the deposition flux (Pinto et al., 2012) is given by:

$$D_i = w_{s,i} c_{i,1} \tag{14}$$

where $c_{i,1}$ is the sediment concentration evaluated at the bottom of the computational cell. In SED, the erosional flux (kg m^{-2} s^{-1}) was parameterised following Ariathurai and Arulanandan (1978):

$$E_i = E_{0,i}(1-\phi) f_i \left(\frac{\tau_m}{\tau_{ce,i}} - 1\right) \text{when } \tau_m > \tau_{ce,i} \tag{15}$$

$$\tau_{ce,i} = \theta_{ce,i} g d_{50,i} \left(\rho_{s,i} - \rho_w\right) \tag{16}$$

where $E_{0,i}$ is the bed erodibility constant (kg m^{-2} s^{-1}); ϕ is the sediment porosity of the top bed layer (dimensionless); f_i is the volumetric fraction of sediment class *i* (dimensionless); and $\tau_{ce,i}$ is the critical shear stress for class i (N m^{-2}). $\theta_{ce,i}$ is the dimensional critical shear stress derived from the critical Shields parameter, and its value is determined following Soulsby and Whitehouse (1997):

$$\theta_{ce,i} = \frac{0.3}{1+1.2 d_{*,i}} + 0.055\left[1 - e^{\left(-0.022 d_{*,i}\right)}\right] \tag{17}$$

In a wave-current coupled model, the bottom shear stress is a combination of the current-induced shear stress and wave-induced shear stress. The latter plays an important role in sediment transport and can thus significantly enhance bottom shear stress, especially in shallow-water regions. This is defined as follows:

$$\tau_w = 0.5 \rho f_{wc} U_w^2 \tag{18}$$

In Eq. (18), U_w is the near-bottom wave orbital velocity, determined from the linear wave theory as:

$$U_w = \frac{a_w \omega}{\sinh kH} \tag{19}$$

where a_w is the wave amplitude and ω is the angular frequency. The combined wave-current friction factor f_{wc} is a function of the relative strength of the currents and waves (Zhang et al., 2004). For current-induced shear stress, the bottom drag coefficient and current-induced bottom stress estimated using the logarithmic law is as follows:

$$C_{db} = \left(\frac{\kappa_0}{\ln\left(\frac{\delta_b}{z_0}\right)} \right)^2 \tag{20}$$

$$\tau_c = \left(\tau_{cx}, \tau_{cy}\right) = \rho C_{db} \sqrt{{u_b}^2 + {v_b}^2} (u_b, v_b) \tag{21}$$

where $\kappa_0 = 0.4$ is the von Karman constant; δ_b is the bottom computational layer thickness (m); and z_0 is the bottom roughness length (m). The wave-current mean bottom stress is then computed according to Soulsby (1997):

$$\tau_m = \tau_c \left(1 + 1.2 \left(\frac{\tau_w}{\tau_c + \tau_w}\right)^{3.2}\right) \tag{22}$$

When wave effects are considered, the bottom roughness length for hydrodynamics and SED will be updated during computation, according to Grant and Madsen (1982); i.e., the wave ripple roughness length is represented by the product of ripple height and ripple steepness multiplied by a constant.

2.4. Model setup

The model domain (Fig. 1) covers the south-central part of Guangdong Province, China. As one of the world's large-scale estuary systems, the PRE comprises three main estuaries: Lingding Bay, Modaomen Estuary (ME) and Huangmaohai Estuary (HE). It includes four main rivers (Xijiang, Beijiang, Dongjiang and Tanjiang), and eight major outlets (from west to east: Yamen, Hutiaomen, Jitimen, Modaomen, Hengmen, Hongqili, Jiaomen and Humen). The horizontal model grid consists of 184,918 triangular elements and 107,262 nodes, with a resolution ranging from 5 to 6 km in the open sea, smoothly varying to approximately 2 km near the coastline before approaching 550 m inside the PRE and finally reaching 100 m in the watercourses (Fig. 1). Vertically, the model uses the new flexible vertical grid system of the Localised Sigma Coordinates with Shaved Cells (LSC^2) developed by Zhang et al. (2015), which is a generalisation of the vanishing quasi-sigma (VQS) suggested by Dukhovskoy et al. (2009). In this study, the number of master grids in the vertical direction was set to 20, starting from 5 to 110 m. The minimum layer number was 12 in the shallowest area where the depth was equal to 3 m, and the maximum was set to 32 layers in the deepest part of the domain.

2.4.1. Datasets

The bathymetry data for the coupled model were constructed using a global and a local dataset. The global dataset, with a resolution of 0.5 arc-min in the open sea, was derived from the General Bathymetric Chart of the Oceans (GEBCO). The local dataset is a digital dataset based on four volumes of the Pearl River Navigation Guide compiled by the Guangdong Maritime Safety Administration. The global tidal model FES2014 (Carrere et al., 2016) was used to generate the harmonic constants for the eight main constituents (M_2, S_2, N_2, K_2, K_1, O_1, P_1, and Q_1) of the open sea boundary nodes. The ocean forcing at the open boundaries, as well as initial conditions, is from daily global HYCOM (Hybrid Coordinate Ocean Model) outputs, including surface elevation, horizontal current velocity, salinity and temperature at different depths (Table 1). The wave model was forced at the ocean boundary by a global hindcast product based on WWIII (Wave Watch III; Rascle and Ardhuin, 2013). Monthly averaged river runoff data and sediment flux data (BCRS, 2007) were provided for the four riverine boundaries. Two types of sediment, fine-grained sediment and sand, were considered. The simulated SSC results used in this study represent both classes of sediment, i.e., the total suspended sediment

concentration.

Table 1

Sources of model forcing fields.

Parameter	Temporal frequency	Spatial resolution	Data source
Initial conditions: T, S, u, v, ssh	Daily	1/12°	HYCOM[a]
Open boundary conditions: T, S, u, v, ssh	Daily	1/12°	HYCOM
Surface forcing: msl, u10, v10, d2m, t2m, ssr, strd[b]	Hourly	0.25°×0.25°	ERA5[c]
Wave boundary conditions: hs, t02, fp, dir, spr[d]	3-hourly	0.5°	WWIII[e]

[a] https://www.hycom.org/data/glbu0pt08/expt-91pt2.

[b] The variables of surface forcing are mean sea-level pressure, 10-m U wind component, 10-m V wind component, 2-m dew point temperature, 2-m temperature, surface net solar radiation and downward surface thermal radiation.

[c] ERA5 is the fifth generation ECMWF (the European Centre for Medium-Range Weather Forecasts) atmospheric reanalysis of the global climate covering the period from January 1950 to present. https://www.ecmwf.int/en/forecasts/datasets/reanalysis-datasets/era5.

[d] Four variables of the wave boundary condition are referred to as significant wave height (SWH), which includes the mean period estimated from the second spectral moment, peak frequency, wave mean direction and directional spread.

[e] https://www.mmnt.net/db/0/2/ftp.ifremer.fr/ifremer/ww3/HINDCAST/GLOBAL/.

2.4.2. Parameters

In this study, the coupled SCHISM-WWM-SED-3D model was used as the baseline model. The main parameters of the hydrodynamic and sediment transport modules are listed in Tables 2 and 3, respectively. The initial proportion condition of bed sediments (fine sediment vs. sand) was set at 0.5 in the upper reaches of the four rivers. Inside Lingding Bay, the proportions were set according to Xia et al. (2008) and simplified appropriately. Outside the coastal area, the proportions decreased gradually to 0.1 following the distribution of bathymetry. To ensure model stability, a time step of 100 s was chosen for every simulation conducted in this study. The same time step was adopted for WWMIII, which meant that the SCHISM hydro module and WWMIII exchanged outputs for every hydrodynamic step. The maximum wave direction in WWMIII was 360°, and this measure was evenly discretised into 36 bins. The low- and high-frequency limits of the discrete wave period were 0.03 and 1.0 Hz, respectively, also equally divided into 36 bins.

Table 2

Model setting.

Parameter (units)	Value	Source
Albedo	0.08-0.18	WRF product[a]
Max. diffusivity ($m^2 s^{-1}$)	1	e.g., Nurser et al. (1999)
Min. diffusivity ($m^2 s^{-1}$)	1×10^{-6}	
Water type	7 (estuarine) for d < 20 m	Jerlov (1976), Wang et al.

	4 (Jerlov type II) for 20 m $\leq d \leq$ 60 m	(2008)
	2 (Jerlov type IA) for d > 60 m	

[a] This WRF (the Weather Research and Forecasting Model) product was provided by the research group of Prof. Shanhong Gao at Ocean University of China, Qingdao.

Table 3

Parameters used in the sediment transport model.

Parameter (units)	Fine sediment	Sand
D_{50} (mm)	0.008	0.08
E_0 (kg m^{-2} s^{-1})	1.0×10^{-5}	1.0×10^{-5}
τ_c (N m^{-2})	0.02	0.1
z_0 (m)	0.001	0.001
w_s (mm s^{-1})	0.08	5.1

3. Baseline experiment for model validation

The coupled SCHISM-WWM-SED-3D was the baseline model used in this study to validate in-situ data from 2007 under normal weather conditions.

3.1. Model skills

For quantitative assessment of model performance, three indices were used. They are the mean absolute error (MAE), root mean squared error (RMSE) and model skill (Willmott, 1981):

$$\mathrm{MAE} = \frac{1}{N}\sum_{i=1}^{N}|X_{mod} - X_{obs}| \tag{23}$$

$$\mathrm{RMSE} = \sqrt{\frac{1}{N}\sum_{i=1}^{N}(X_{mod} - X_{obs})^2} \tag{24}$$

$$\mathrm{Skill} = 1 - \frac{\sum_{i=1}^{N}|X_{mod}-X_{obs}|^2}{\sum_{i=1}^{N}(|X_{mod}-\overline{X_{obs}}|+|X_{obs}-\overline{X_{obs}}|)^2} \tag{25}$$

where X_{mod} and X_{obs} are the modelled and observed values, respectively, which are compared with $\overline{X_{obs}}$ (overbar indicates the time mean value over the number of observations, N). The model skill index ranges from zero to unity, with one indicating perfect agreement and zero indicating no agreement.

3.2. Tides

A comparison between the model results and observations for surface elevation was made at three tidal gauge stations (T1, T2 and T3; Fig. 1). The data used for the model skill assessment of T2 was from August 2007, showing good performance with a skill score of 0.99 (Table 4). The simulated and observed variables at Station T2 (Fig. 2) show that the PRE was dominated by irregular semidiurnal tides, with two high tides and two low tides during a lunar day. For all three stations, the model results match observed tidal elevation variability reasonably well, with a range of 0.07–0.18 m for both MAE and RMSE, although the observed data at T1 and T3 covered only two days.

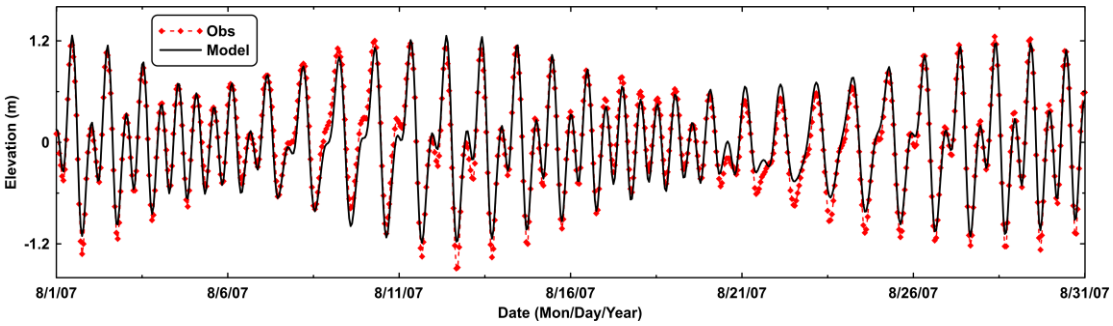

Fig. 2 Comparison of observed and simulated elevation at Station T2 during 1–31 August 2007.

Table 4

Model skills for simulating tides.

Station	T1	T2	T3
MAE (m)	0.14	0.10	0.07
RMSE (m)	0.18	0.13	0.09
Skill	0.98	0.99	0.99

3.3. Significant wave height

The model results of SWH were consistent with the five-day observations at Station T2 from 13 August to 18 August 2007 (Fig. 3). The observed SWH was between 0.15 and 0.75 m, with an average of 0.35 m. Some discrepancies between the model and observed SWH may have been due to the limited spatial and temporal resolution of the atmospheric forcing used in the simulation and due to the WWIII boundary data.

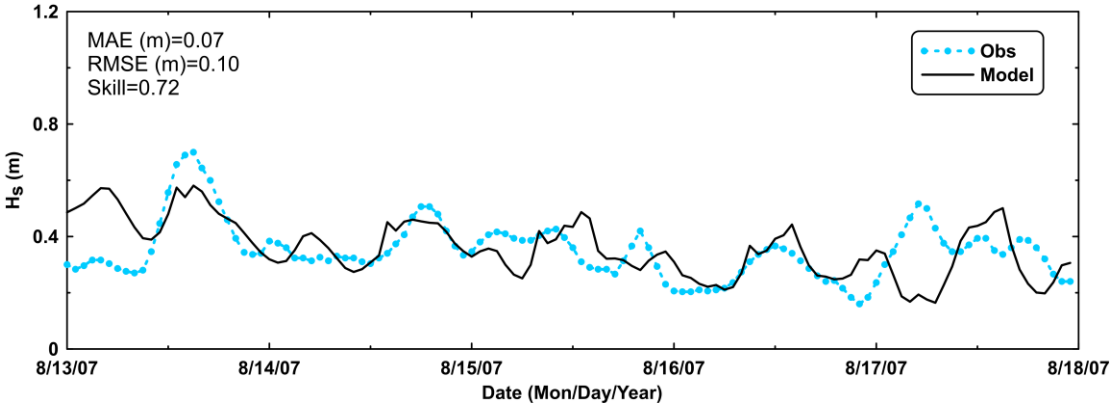

Fig. 3 Comparison between observed and simulated SWH at Station T2 during 13–18 August 2007.

3.4. Currents

In situ data were used to validate the simulated current velocity, salinity and SSC at four stations (C1–C4; Fig. 1), although the data only covered a period of approximately two days. Current velocities in the eastward (u component) and northward (v component) directions in the surface and bottom layers were assessed (see Fig. 4, for example). The mean model skills (variable V_a) for current velocities at the four stations, including both u and v components in the surface and bottom layers, are listed in Table 5. The simulated northward velocities in the surface layer coincided better with the

observed values than the eastward velocities, achieving a mean velocity skill of 0.91, mainly because the northward was greater than the eastward velocity. In the bottom layer, the skills of both velocity components were close to 0.78, indicating that the model reproduced the bottom velocity field well.

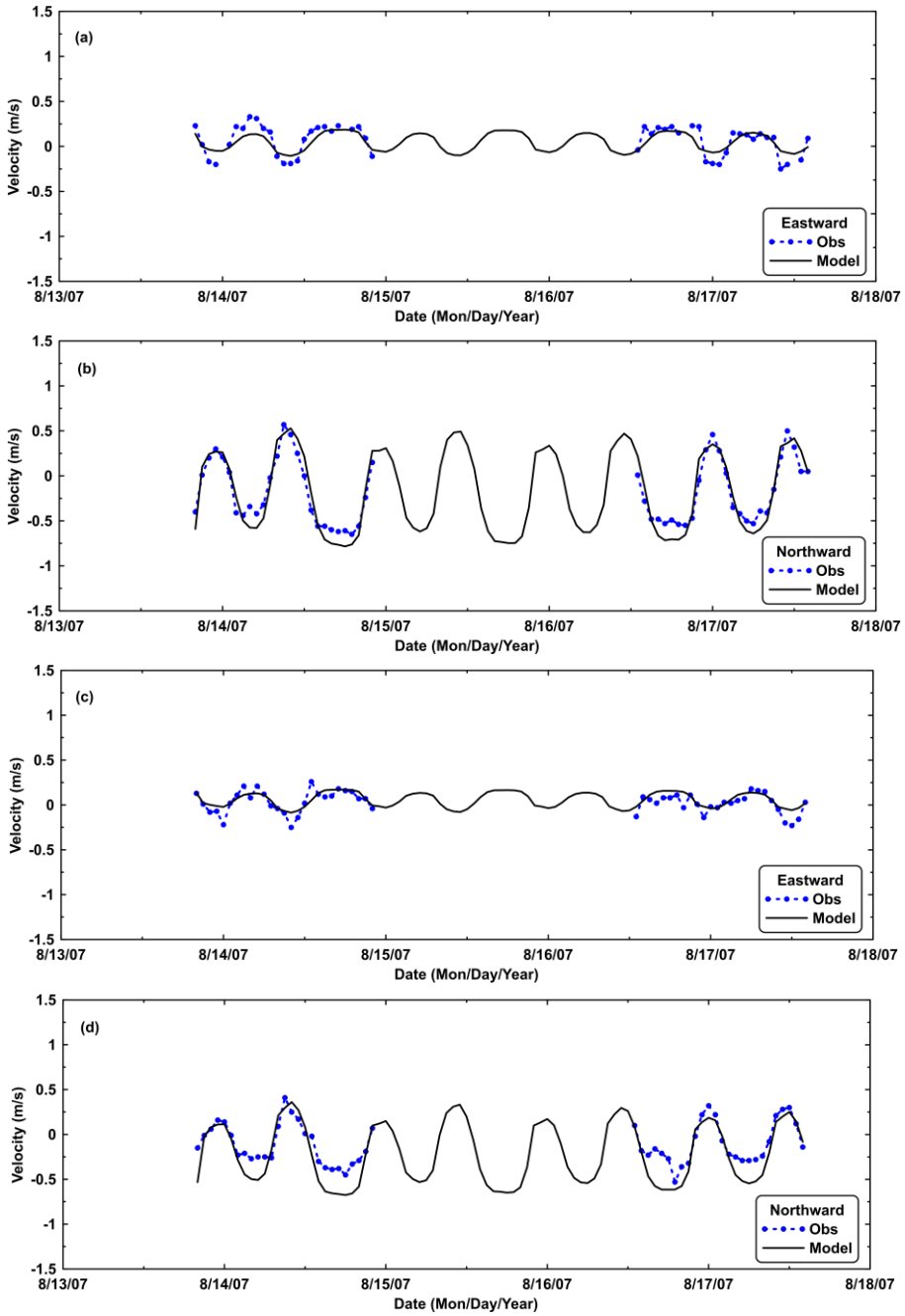

Fig. 4 Comparison of surface (a, b) and bottom (c, d) velocities between observations and model results at Station C2 during 13–18 August 2007.

3.5. Salinity

Due to the influence of the summer monsoon, the flood period of the Pearl River is normally from April to September each year, and the dry period is from October to March of the following year. The runoff during the flood period accounts for 75–85% of the annual amount. For coastal areas with water depths of less than 50 m, the distribution of surface salinity is significantly affected by the Pearl River diluted water. The mean model skills of salinity at the surface and bottom layers of the four stations are

presented in Table 5. In August 2007, the salinity of stations C1 and C2 (missing observed data), located at the outlets influenced by both the Beijiang and Xijiang, had a small range of 0.10–0.43 in both the surface and bottom layers. The observed surface and bottom salinity data at Station C3 during the two days (Fig. 5) showed a large fluctuation range of 10.0–20.0 and 12.0–31.0, respectively. This is because the location of Station C3 was affected by a strong salinity front which was formed by the mixing of diluted water from the northern outlets and local shelf water. Station C4 was dominated by high-salinity ocean water, resulting in averaged values of 24.0 and 34.0 for surface and bottom salinity, respectively.

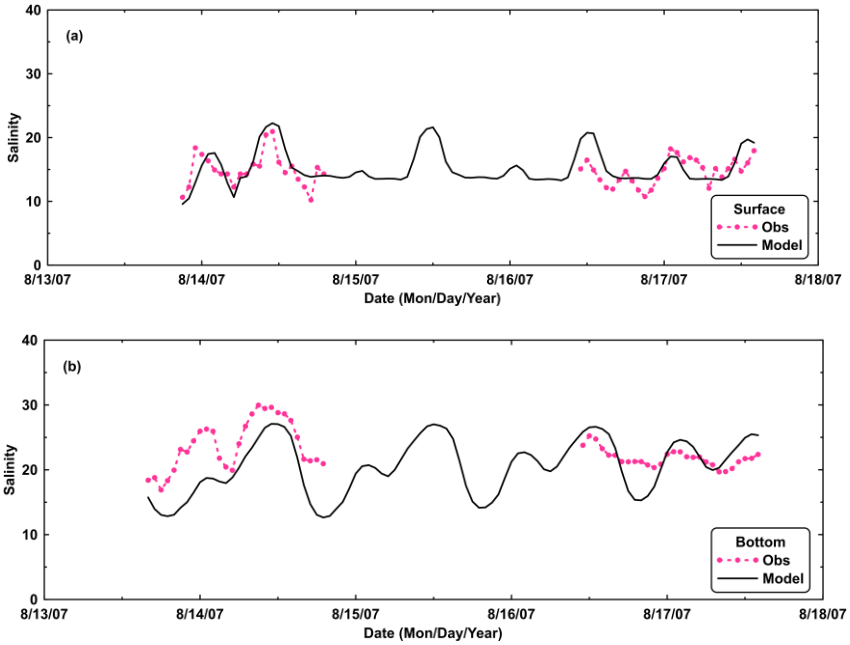

Fig. 5 Comparison of surface (a) and bottom (b) salinity between observations and model results at Station C3 during 13–18 August 2007.

3.6. Suspended sediment concentration

The mean model skills of the SSC in the surface and bottom layers of the four stations are listed in Table 5. The SSC values in the surface and bottom layers at the four stations matched the in-situ data (see Fig. 6, for instance). The mean values of the observed surface SSC were 0.082, 0.087, 0.116 and 0.008 g/L, which increased to 0.135, 0.111, 0.140 and 0.029 g/L at the bottom, respectively. In view of the simulated results, almost all the SSC came from the fine sediment during normal weather days.

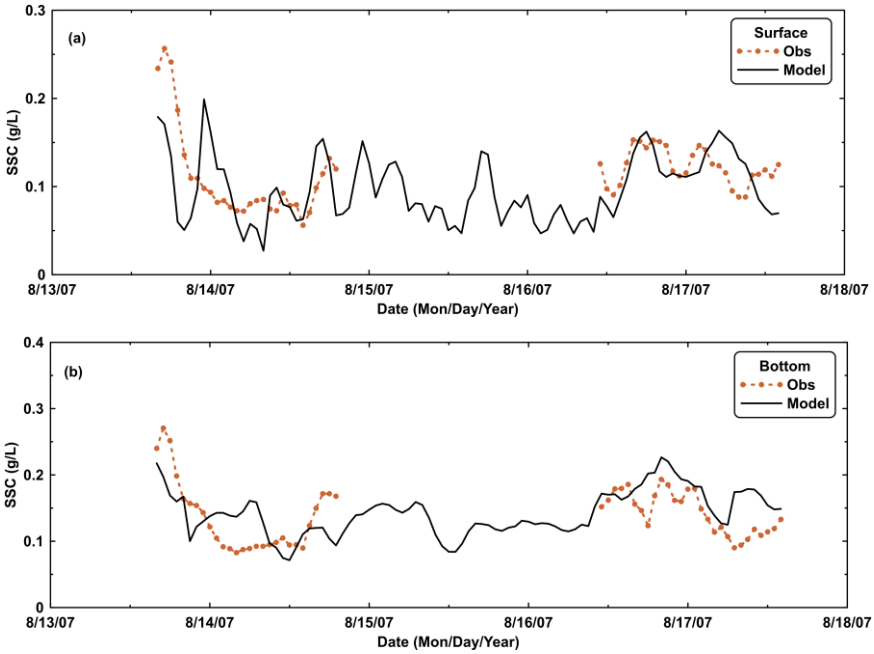

Fig. 6 Comparison of surface (a) and bottom (b) SSC between observations and model results at Station C3 during 13–18 August 2007.

Table 5

Model skills for simulating velocity, salinity and SSC.

Station	C1			C2			C3			C4		
Variable	V_a	Sal	SSC	V_a	Sal	SSC	V_a	Sal	SSC	V_a	Sal	SSC
MAE (m/s; -; g/L)	0.19		0.024	0.11		0.025	0.18	2.99	0.03	0.18	1.04	0.0035
RMSE (m/s; -; g/L)	0.22		0.032	0.13		0.029	0.22	3.72	0.04	0.23	1.32	0.0047
Skill	0.86		0.41	0.87		0.44	0.82	0.70	0.66	0.73	0.67	0.67

4. Baseline experiment results

We verify the feasibility of the coupled model during Typhoon Mangkhut using both in situ and Moderate Resolution Imaging Spectroradiometer (MODIS) data. Then, we analyse variations during three different periods of the typhoon.

4.1. Brief description of Typhoon Mangkhut

Typhoon Mangkhut was a record-breaking storm among the typhoons that hit the PRE in recent years because of its intensity, scale, and serious wind and rainfall impacts. Its moving path (Fig. 7) followed the majority of historical typhoon tracks in this region (Yang et al., 2019). The storm was formed on 7 September 2018, quickly intensified over the next two days and finally strengthened to a super typhoon at 0:00 UTC on 11 September. Typhoon Mangkhut battered Cagayan, Philippines, at 18:00 UTC on 14 September, with a central pressure of 910 hPa and a maximum wind speed of 65 m/s (according to the CMA data; http://typhoon.weather.com.cn/). After passing over the Philippines, the

weakened Typhoon Mangkhut gathered more energy from the SCS and reconstructed its eye. Subsequently, it made its second landfall as a severe typhoon in Jiangmen, Guangdong, China, with a maximum wind speed of 48 m/s and central pressure of 955 hPa at 9:00 UTC on 16 September 2018.

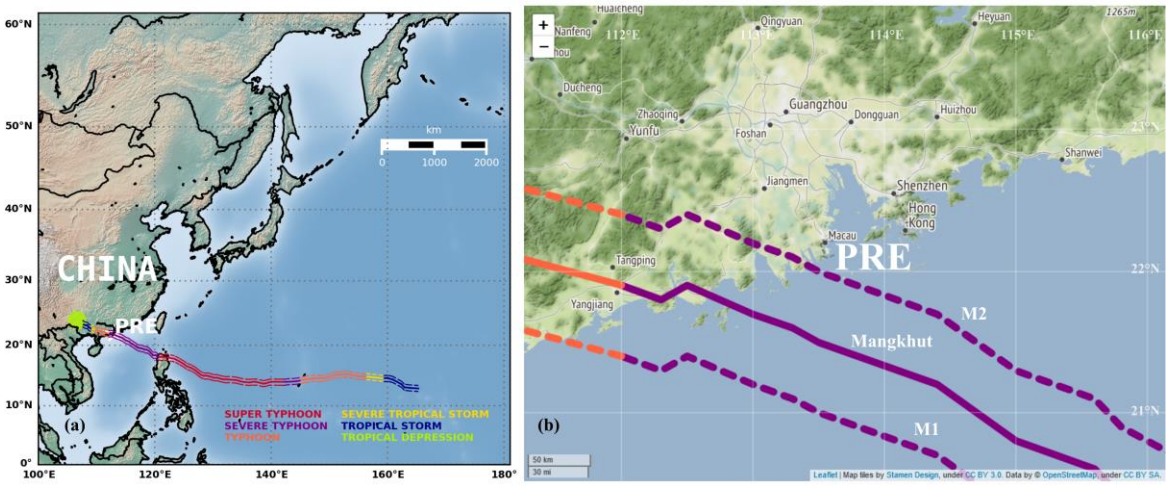

Fig. 7 Path of Typhoon Mangkhut in 2018 (solid line) and simulated typhoon paths of Case 5a (M1) and Case 5b (M2) described in Section 5 (dash lines).

4.2. Verification of typhoon surge

The ECWMF's ERA5 reanalysis was used as forcing at the air-sea interface, except that the WRF product with higher resolution was applied during the entire typhoon period to improve the precision of typhoon simulation. Note that the observed sea level at four tidal gauge stations (H1–H4 in Fig. 1) also captured Typhoon Mangkhut from 16:00 UTC on 14 September to 3:00 UTC on 18 September 2018 (Fig. 8). To show the impact of Typhoon Mangkhut, we verified predicted storm surges at the four tidal gauge stations. The predicted surge height was obtained by subtracting the predicted astronomical tidal level, which was based on an 11-month (from June 2019 to May 2020) harmonic analysis of tides (using 63 tidal constituents) from the measured tidal level. It was obvious that Typhoon Mangkhut had a severe impact on the coastal area of the PRE, with high surges of 2.78, 3.13, 2.29 and 3.22 m, respectively, at the four stations from north to south. The model successfully reproduced the surges of Typhoon Mangkhut, with high skills of 0.94, 0.98, 0.90 and 0.97 at the four stations, respectively (Table 6).

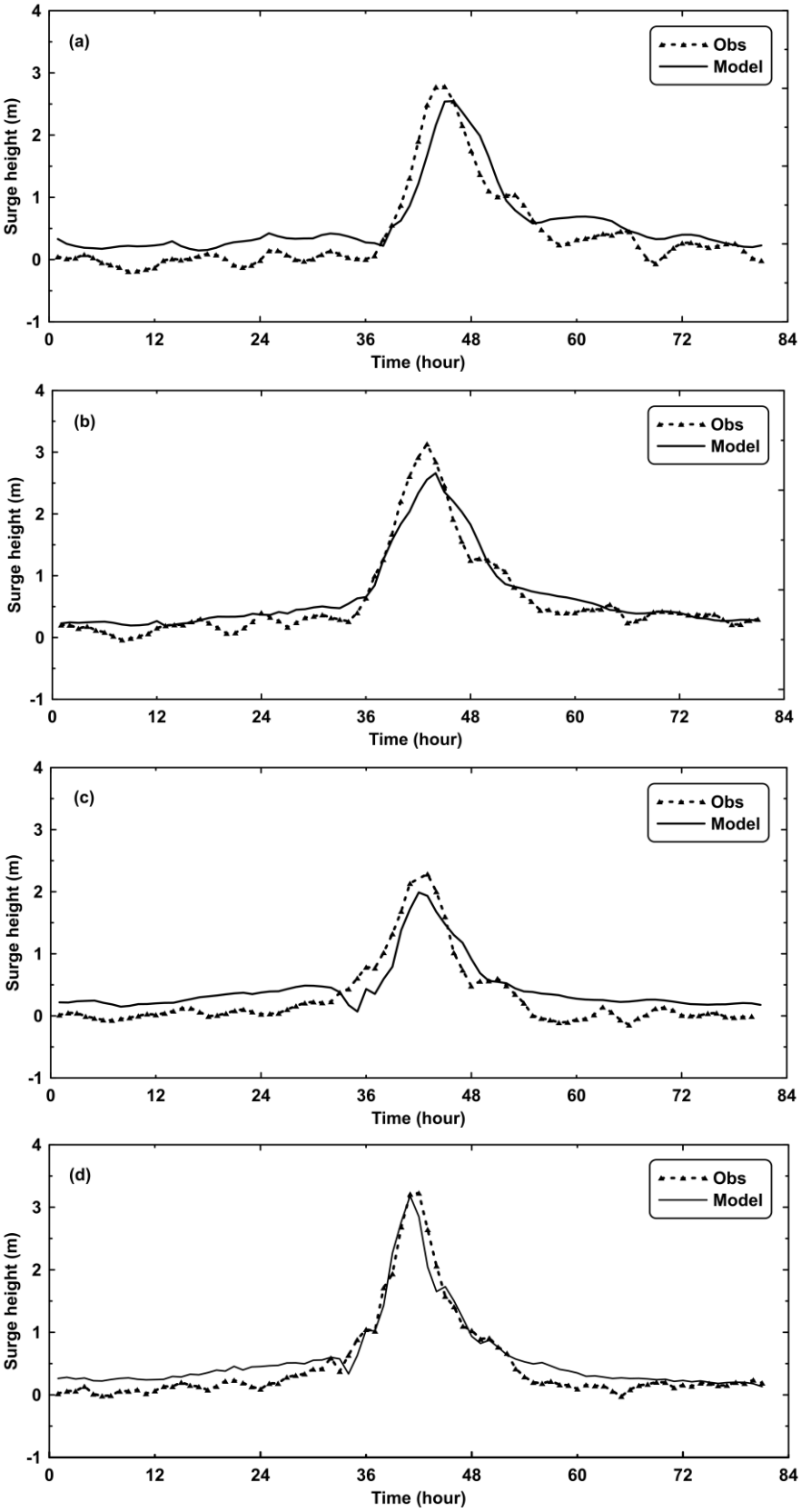

Fig. 8 Comparison of surge height at H1 (a), H2 (b), H3 (c) and H4 (d) during 81 h starting from 16:00 UTC, 14 Sep. 2018.

Table 6

Model skills for simulating storm surges.

Station	H1	H2	H3	H4
MAE (m)	0.26	0.15	0.25	0.18
RMSE (m)	0.30	0.20	0.27	0.23
Skill	0.94	0.98	0.90	0.97

4.3. Surface SSC verification after typhoon decay

Although we have no data from Lingding Bay or from the west coast area due to dense typhoon clouds, we found two MODIS ocean colour images to validate the simulated surface SSC at 2:55 (Fig. 9a, Terra) and 6:05 (Fig. 9b, Aqua) UTC, 18 September 2018 after Typhoon Mangkhut decayed for approximately 18 h and 21 h, respectively. According to Miller and McKee (2004), a significant relationship was observed between the total suspended matter concentration (mg/l) and atmospherically corrected MODIS Terra band-1 data. A correction coefficient was selected after carefully comparing Fig. 4 in Miller and McKee (2004) and MODIS Terra ocean colour data. Based on this magnification factor, a new linear relationship was acquired to fit and map the distribution of surface SSC with both MODIS Terra and Aqua data.

During the calm post-typhoon period in the PRE, the spatial distribution of suspended sediments of the coupled model were fairly consistent with the ocean colour data (Fig. 9). Overall, the concentration gradient of suspended sediments in the surface layer exhibited a northeast-southwest trend following the change in water depth. In both ocean colour images and model results, it showed clearly that the relatively high SSC located near 113.8°E, 21.8°N offshore of the PRE decreased from 0.08–0.09 g/L to 0.05–0.06 g/L within 3 h after Typhoon Mangkhut left the area. At these two moments, the high-SSC zone expanded northeastward along the coast in both MODIS and model results, although the model results were slightly higher than those in the MODIS images. The discrepancies probably occurred because of inaccurate values of seabed thickness and seabed fraction used for these two types of sediments. The model skills of surface SSC are 0.68 and 0.61, respectively, compared to MODIS Terra and Aqua data. Using the baseline setting, the model reasonably captured the general structure of hydrodynamic and transport variations and can be used to study the physical mechanisms of sediment transport during typhoons.

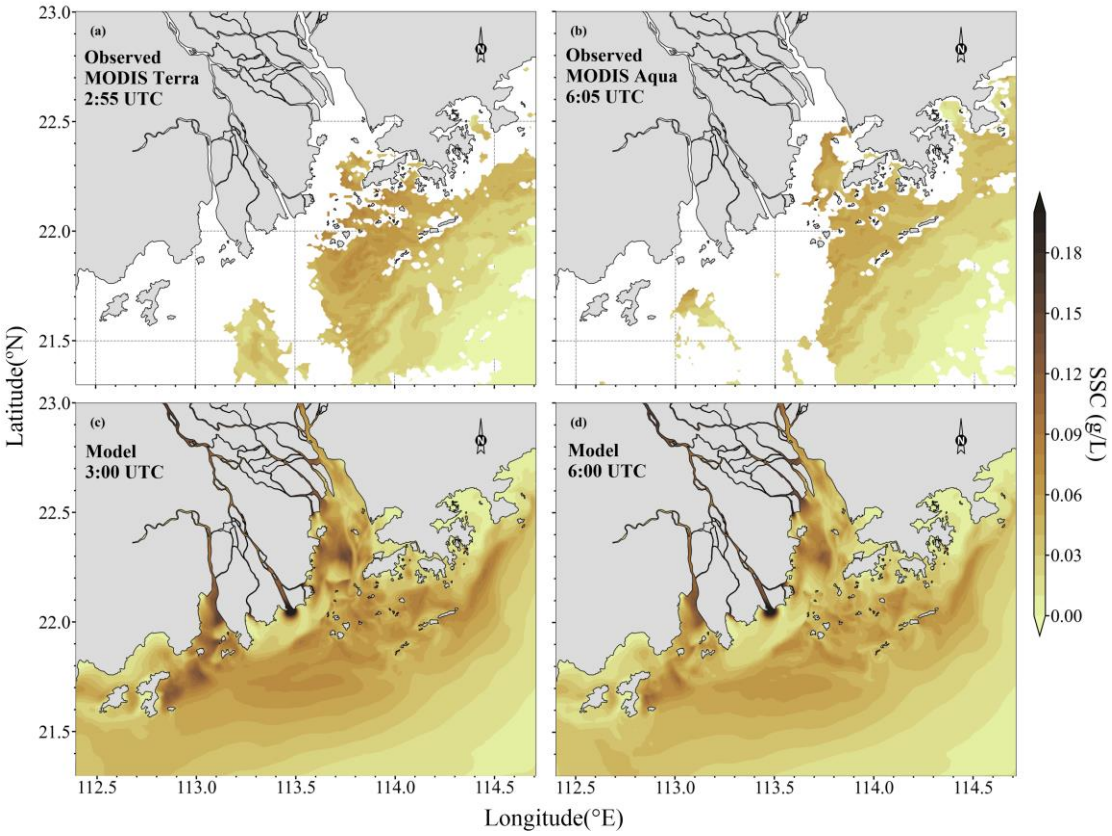

Fig. 9 Comparison of ocean color data* and model results at two different times on 18 September 2018 during Typhoon Mangkhut's decay.

(* https://oceancolor.gsfc.nasa.gov/cgi/browse.pl?sen=amod)

4.4. Analysis of model results averaged during each of the three periods

The model results were divided into three phases using the M_2 tidal cycle (12.42 h) as the interval, starting from the PRE which was obviously affected by Typhoon Mangkhut. The first period was from 11:00 to 23:25 UTC on 15 September 2018 (P1). The second covers the landfall process of Typhoon Mangkhut from 23:25 UTC on 15 September to 11:50 UTC on 16 September 2018 (P2). The third period starts after the landfall, from 11:50 UTC on 16 September to 0:15 UTC on 17 September 2018 (P3). The time-averaged model results for the periods P1, P2 and P3, respectively, were then used to reveal the changes in the distribution of SSC, SWH, near-bottom wave orbital velocity and bottom shear stress.

4.4.1. Averaged model results in P1

In P1, the averaged distributions of both surface (Fig. 10a) and near-bottom (20th layer) SSC (Fig. 13a) resembled the normal state where the areas of concentration greater than 0.10 g/L reached 667 and 1,288 km^2, respectively. High concentrations were mainly distributed on the WS inside Lingding Bay, in the four western outlets (Modaomen, Jitimen, Hutiaomen and Yamen) and the HE, and along the coastal zone to the west of the HE. The nearshore wind field presented a northerly wind with a mean speed below 10 m/s, which indicated that the typhoon was on its way from the southeast (Fig. 10b). Correspondingly, the mean current forced by the wind flowed southwestward, and the averaged distribution of SWH was highly consistent with the strength of the typhoon wind. The average value of

the near-bottom wave orbital velocity began to rise across the whole domain as the wind speed increased, but especially in the shallow-water area, owing to the effect of topography (Fig. 10c). In this period, the nearshore distribution of bottom shear stress (Fig. 10d) resembled the distribution of SSC, while in some parts of the deeper waters, the typhoon had an increased influence.

4.4.2. Averaged model results in P2

In P2, the above-mentioned variables showed obvious variations. Compared to the results in P1, the area of the averaged surface SSC (Fig. 11a) at a concentration greater than 0.10 g/L increased from 667 to 4,634 km^2. The maximum averaged SSC occurred at the Modaomen outlet in both surface and near-bottom layers, respectively, at 0.66 and 0.71 g/L (Fig. 13b). During P2, the maximum averaged wind speed reached ~26 m/s, and the surface current field was cyclonic, but its centre location lagged behind that of the typhoon (Fig. 11b). The average SWH along the coastline clearly increased by approximately 1.5 m, with the mean sea level reaching ~1.0 m in the PRE and around the western outlets. Meanwhile, both the near-bottom wave orbital velocity (Fig. 11c) and bottom shear stress (Fig. 11d) increased relatively, which indicated that the bottom current had already exceeded the critical velocity for sediment resuspension. Because of the shallow water depth, the effect of waves on sediment in the WS was greater than that in the East Shoal (ES). The bottom shear stress along the 30-m isobath in the west coast area between the ME and HE showed larger values, but the distribution of SSC did not present similar characteristics.

4.4.3. Averaged model results in P3

After Typhoon Mangkhut made landfall, the averaged wind direction in the domain was southeasterly, and the intensity remained strong (Fig. 12b). During the decay of the typhoon, the near-bottom wave orbital velocity (Fig. 12c) and bottom shear stress (Fig. 12d) significantly declined, while the SSC continued to increase. The area of the averaged surface SSC, at a concentration greater than 0.10 g/L during P3, reached 9,447 km^2, which doubled the area during P2 (Fig. 12a). In vertical profile, the horizontal distribution characteristics of the averaged SSC were similar in every layer owing to the intensified mixing induced by the typhoon. The variation in SSC had a time lag compared with other dynamic fields, reaching a maximum value 1 h after landfall. Unlike the rapid response of the surface flow field to the typhoon, the current direction of the near-bottom layer was different (i.e., still flowing southwestward) because of the lag caused by the interval needed for wind to transfer momentum to the entire water column (Fig. 13c). This drove the suspended sediment of the corresponding layer to diffuse and transport southwestward.

4.4.4. Averaged model results for sand

Although Typhoon Mangkhut made a significant contribution to the distribution of SSC in both surface and near-bottom layers, the concentration of suspended sand (Fig. 14) eroded by typhoon winds and waves was quite small compared to the total suspended sediment concentration. In P2, the suspended sand area at a concentration greater than 0.01 g/L in the near-bottom layer (Fig. 14b) was about 717 km^2, but that at the surface was only 0.83 km^2 (Fig. 14a). However, the distributions of sand and bottom shear stress corresponded well. This explains why the enhanced bottom shear stress under typhoon conditions also had a significant effect on the erosion and migration of sand.

Combined with the earlier results, this feature illustrated that the increased total suspended sediment concentration in the area with depths shallower than 20 m, especially in the ME, the HE and

along the entire west coast, was dominated by the regional erosion of fine sediment, which was caused by near-bottom wave orbital velocity and bottom shear stress. For the deeper coastal zone at depths between 20 and 30 m offshore of the western coast, the high total suspended sediment concentrations mainly contributed to the fine sediment transported from the upper and middle estuaries by southwestward advection.

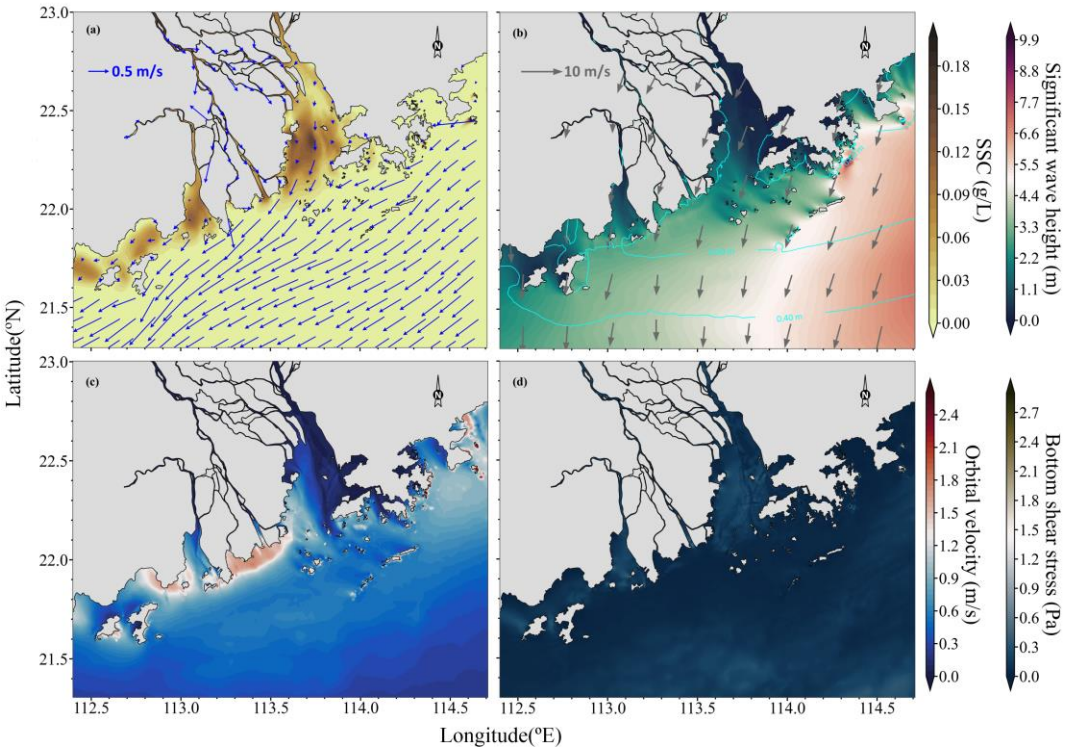

Fig. 10 Averaged model results in P1.

SSC distribution and currents of surface layer (a); SWH, wind, and elevation (b); near-bottom wave orbital velocity (c); bottom shear stress (d)

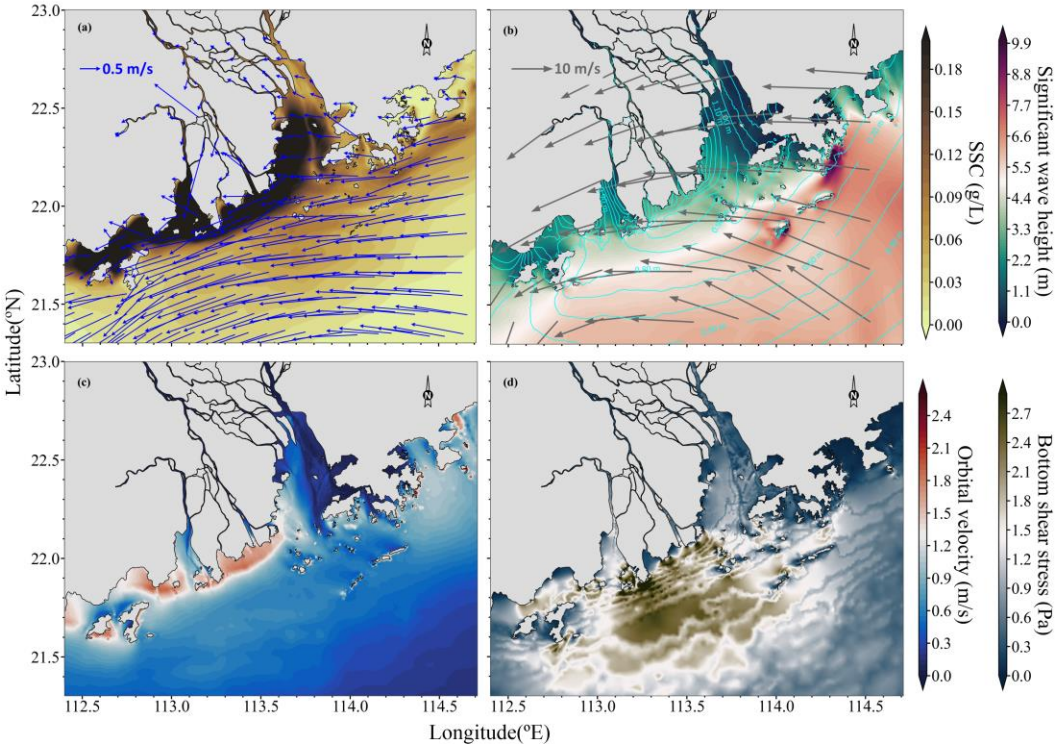

Fig. 11 Averaged model results in P2.

SSC distribution and currents of surface layer (a); SWH, wind, and elevation (b); near-bottom wave orbital velocity (c); bottom shear stress (d)

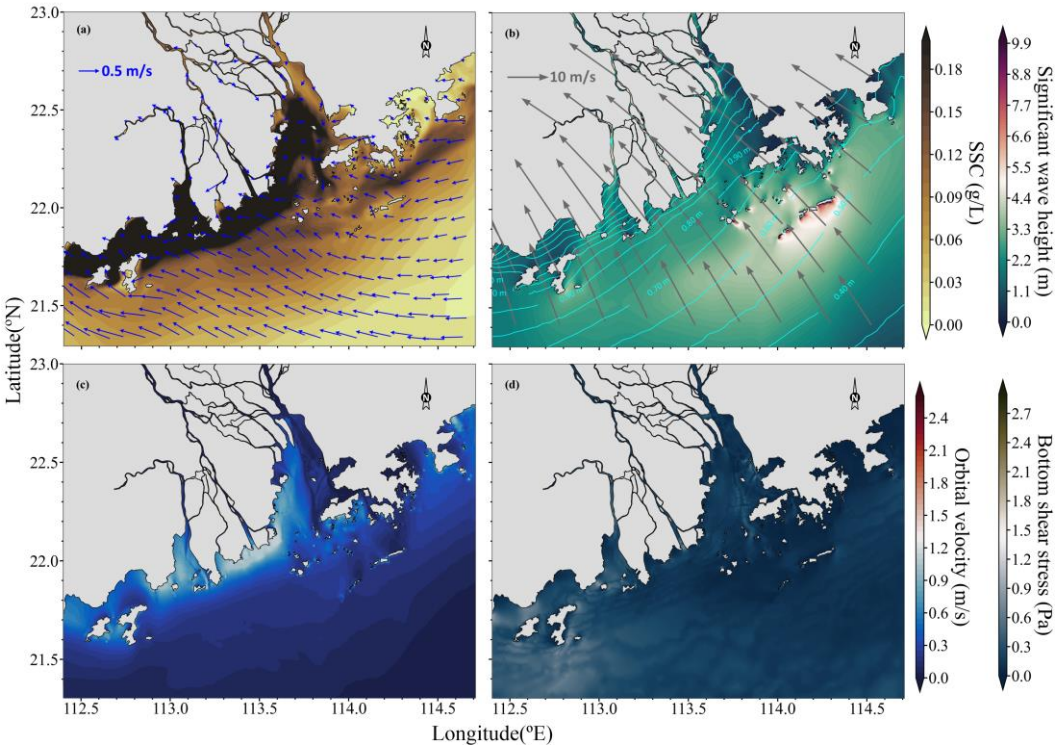

Fig. 12 Averaged model results in P3.

SSC distribution and currents of surface layer (a); SWH, wind, and elevation (b); near-bottom wave orbital velocity (c); bottom shear stress (d)

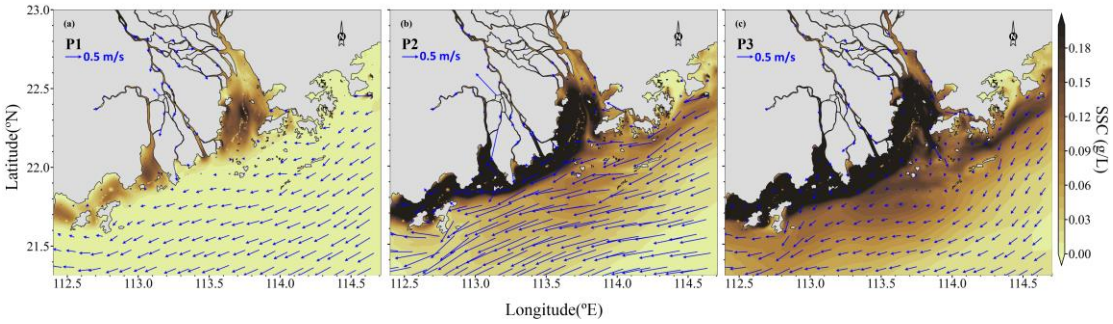

Fig. 13 Averaged SSC and currents of near-bottom layer: P1 (a), P2 (b) and P3 (c).

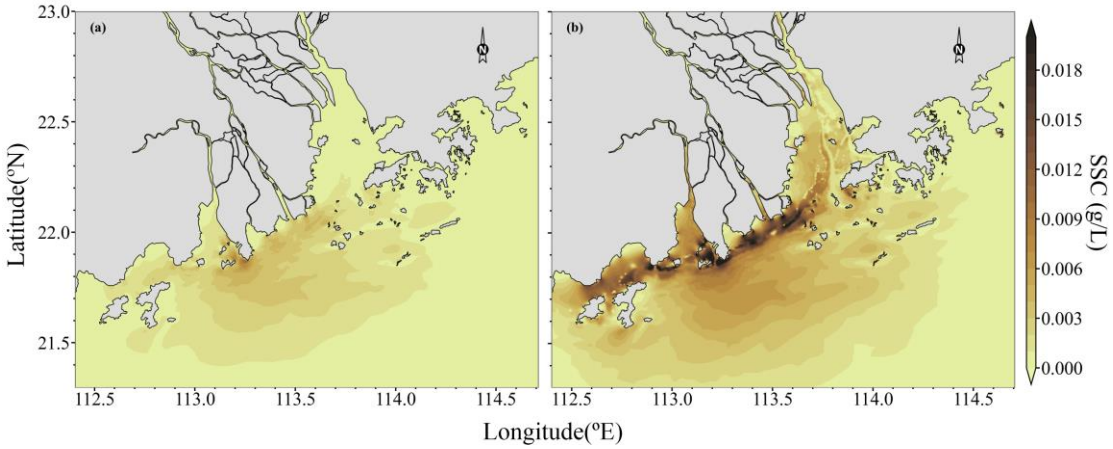

Fig. 14 Averaged distributions of sand at surface (a) and near-bottom layers (b) in P2.

5. Discussion

To gain insights into sediment transport during Typhoon Mangkhut, we carried out five sensitivity experiments (Table 7), in addition to the baseline experiment (Case 1). In Case 2, the wave effects under the typhoon were not considered. To isolate the impact of the typhoon wind, the atmospheric forcing in Case 1 was replaced by the five-year-averaged wind data of 2015–2019; together with the wave boundary conditions of normal weather, we used two cases: Case 3 (with wave effects) and Case 4 (no wave effects). Cases 5 and 6 were designed to explore the sensitivity of the SSC distribution by changing the track and intensity of Typhoon Mangkhut, respectively.

Table 7

Base and sensitivity experiments.

Exp	Setup
Case 1	Baseline experiment, with 3D coupled baroclinic SCHISM-WWM-SED-3D, described in Section 4
Case 2	Same as Case 1, except without WWMIII module
Case 3	Same as Case 1, except using average of five-year (2015–2019) wind data as atmospheric forcing and wave boundary condition to remove the impacts of Typhoon Mangkhut
Case 4	Same as Case 3, except without WWMIII module
Case 5a	Same as Case 1, except the typhoon path shifted southward by 0.5°(M1 in Fig. 7b)
Case 5b	Same as Case 1, except the typhoon path shifted northward by 0.5°(M2 in Fig. 7b)
Case 6a	Same as Case 1, except the typhoon intensity (air pressure and wind speed) equal to the original intensity multiplied by a coefficient based on the ratio of the averaged wind speed between Case 5a and Case 1 (varying with nodes, the average values for u and v components are 0.84 and 0.78, respectively)
Case 6b	Same as Case 6a, except using a coefficient based on the ratio of the averaged wind speed between Case 5b and Case 1 (varying with nodes, the average values for u and v components are 1.14 and 1.29, respectively)

5.1. Role of waves under extreme weather conditions

Here, we analyse the wave-current interaction and its direct effects under extreme weather conditions. Then, we analyse its effect on sediment budgets in Lingding Bay during different time periods of Typhoon Mangkhut.

5.1.1. Wave-current interaction and its effects

During P2, the averaged distribution of SSC in Case 2 (Fig. 15a) shows a significant increase when the strong wind moves toward the coastal area, similar to that in Case 1 (discussed in Section 4). The extent of erosion increased sharply, with almost the entire Lingding Bay and the west coast of the PRE covered by suspended sediments. Likewise, the distribution in the near-bottom layer had similar characteristics to those in the surface layer and was even more noticeable in the concentration level of the offshore area (not shown). However, the surface and near-bottom maximal concentrations of Case 1 (0.66 and 0.71 g/L, respectively) were 1.5 and 1.3 times larger, respectively, than those of Case 2 (0.44 and 0.55 g/L, respectively). Correspondingly, the surface and near-bottom suspended areas at a concentration greater than 0.10 g/L in the averaged distribution in Case 1 were 645 and 840 km^2 larger,

respectively, than those in Case 2 (3,989 and 4,131 km^2, respectively). During P1 and P3, the SSC distributions in the surface and near-bottom layers in Case 1 also increased compared with those in Case 2 (not shown). These results indicate that the wave-current interaction induced by intense typhoon winds greatly increased the erosion of bottom sediments.

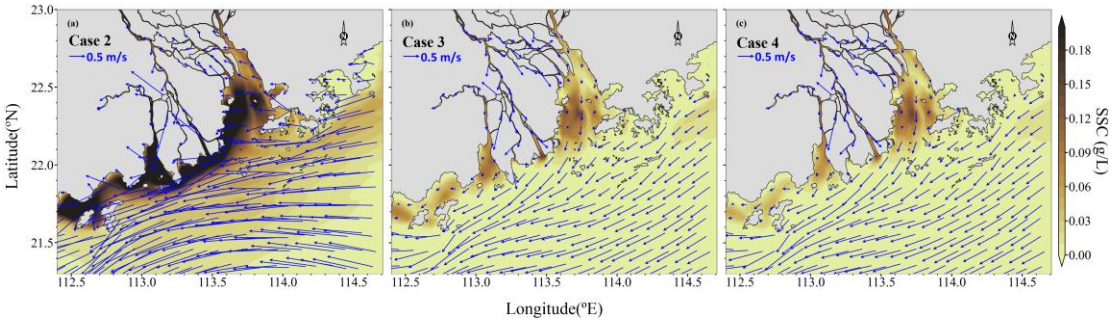

Fig. 15 Surface distributions of SSC and currents during P2 for Cases 2−4.

To reveal the cause of these results, we show the differences in bottom shear stress, surface SSC distribution and current velocity between Cases 1 and 2 during the three periods in Figs. 16 and 17. The bottom shear stress initially increased by 0.1 Pa in P1 (Fig. 16a) because the wind waves were only active near the open boundary of the domain. The differences in the averaged SSC and current velocity between Cases 1 and 2 were also insignificant (Fig. 17a). In P2, the wind waves caused by Typhoon Mangkhut showed powerful effects on bottom shear stress, particularly in the area shallower than 30 m, with the differences reaching 0.5 Pa (Fig. 16b). Therefore, the erosion of SSC due to enhanced bottom shear stress under wave-current interaction increased correspondingly, resulting in the difference in the averaged SSC distribution becoming larger during P2 (Fig. 17b). The maximum differences, reaching 0.15 g/L, were located offshore of the western outlets and along the west coast of the HE where the maximal SSC values were. However, the westward current significantly decreased in the same period because of the joint effect of wave radiation stress and enhanced bottom shear stress. Similar differences were observed in the near-bottom layer (not shown). During P3, although the differences in bottom shear stress show negative values ranging from 0.15 to 0.20 Pa in the deeper coastal zone at depths of approximately 30 m offshore of the HE, the other areas still display slightly positive differences (Fig. 16c). The sediments eroded by wave-current interaction showed sustained local erosion inside the western outlets and along the west coast of the HE due to the movement of Typhoon Mangkhut. The wave-enhanced erosion continued to increase during this period (Fig. 17c), while the differences in the current field continued to block westward sediment transport and increase suspended sediments in the area along the 20-m isobath in the ME. This illustrates that when the sediments moved westward under typhoon forcing, wave-current interaction played a key role in continuously decreasing the westward transport of suspended sediments, which resulted in the generation of a high-concentration area at the 20-m isobath in the ME.

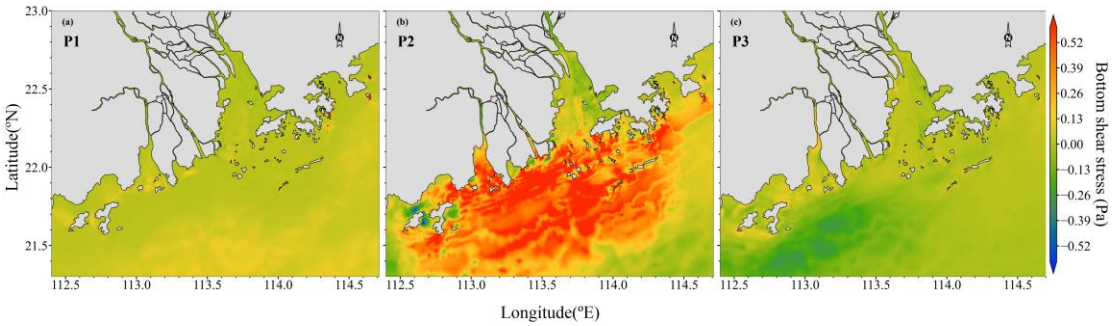

Fig. 16 Differences of bottom shear stress between Cases 1 and 2 in three periods.

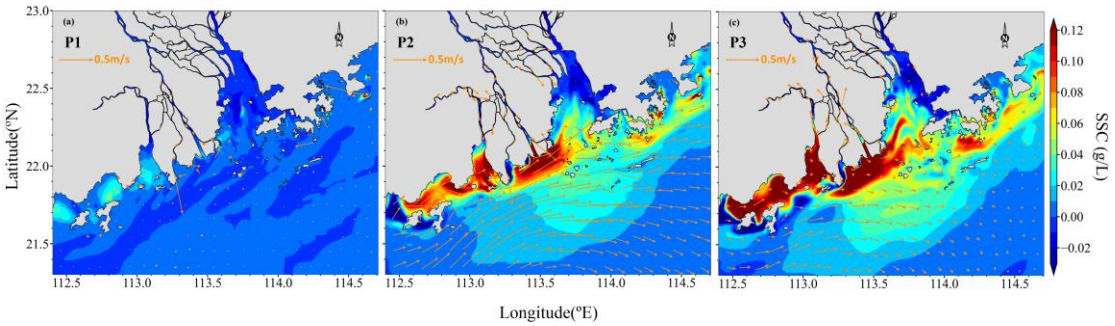

Fig. 17 Differences of SSC and currents between Cases 1 and 2 at the surface in three periods.

The suspended sediment flux (vectors in Fig. 18) is the product of the SSC and current field. Although the maximal difference in suspended sediment flux between Cases 1 and 2 (Figs. 18a and 18b) is also seen in the ME, with a value of ~0.26 kg/(m^2·s), the sediment transport flux displays some difference in the areas with a high concentration of averaged SSC. Therefore, we found that it was difficult to determine the locations with maximum intensity of sediment transport through the averaged SSC distribution, which was attributed to the altered current field induced by wave-current interaction under typhoon conditions.

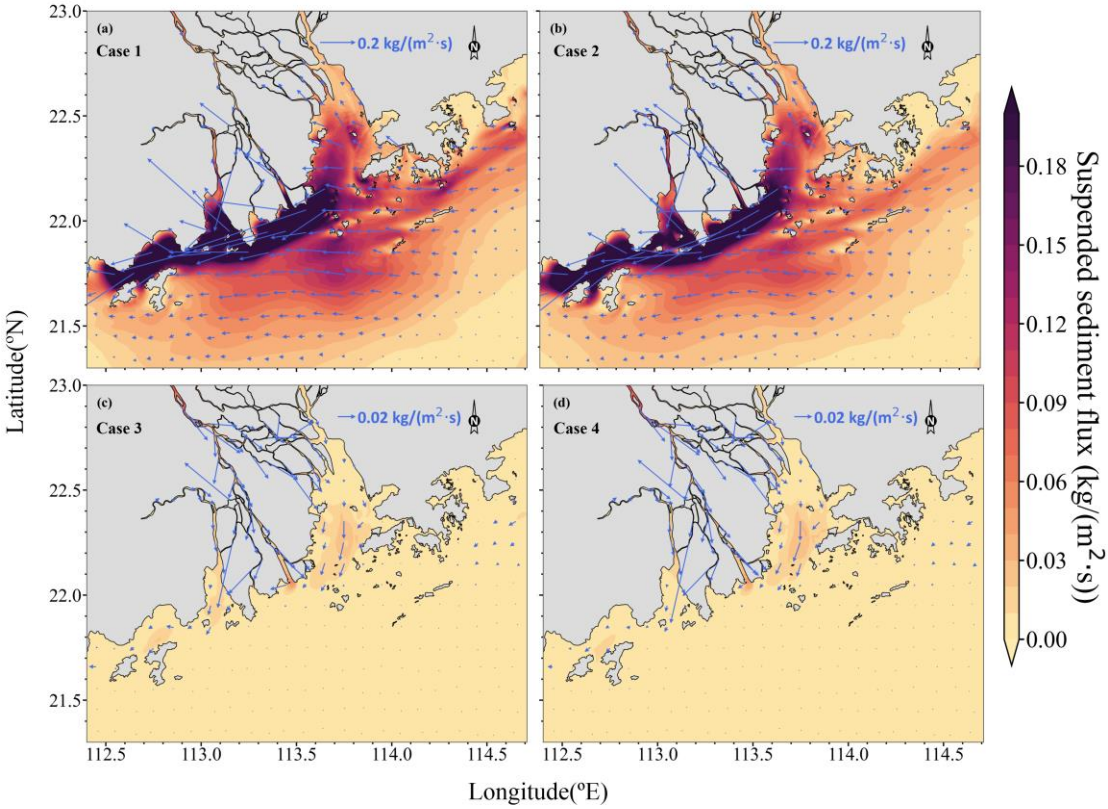

Fig. 18 Average surface suspended sediment fluxes of four cases in P2.

5.1.2. Sediment budgets in Lingding Bay

To investigate total sediment budgets that considered suspended load sediment exchanges among different horizontal areas under wave-current interaction, we selected transects E1 (west entrance) and E2 (east entrance), similar to those in Zhang et al. (2021). We added transect E3 along the west channel, while we added transects E4 and E5 to the northwest and north outlets, respectively. As a result, from south to north, Lingding Bay was divided into two parts (Fig. 19). Transects E1 and E2 are the west and east entrances, respectively, between Lingding Bay and the lower estuary, while transects E4 and E5 are the west and east entrances, respectively, between Lingding Bay and the upstream outlets. In addition, transect E3 between the west and east sides of Lingding Bay is divided into two parts by Neilingding Island, while transect E1 is divided into two parts: the shoal on the west and the channel on the east. We start with Case 1. During the typhoon, the total suspended load sediment transport across transects E1, E3 and E4 represented the sediment budget on the west side of the estuary; similarly, the total sediment transport across transects E2, E3 and E5 represented the sediment budget on the east side of the estuary.

In Case 1 (with waves), sediment transport mainly occurred in the area on the west side of Lingding Bay and south of Point B when initially affected by the typhoon. Approximately 60% of these sediments were transported southwestward following the mean flow in the shoal on the west side of Point A, while the remainder were transported northward in the channel on the east side of Point A (Fig. 19a). A small number of sediments were imported into Lingding Bay from the east entrance and from upstream outlets in the northwest and north across transects E2, E4 and E5, respectively. As a result, the sediment budgets for the west and east sides of the bay were -11.93 and +11.70 kt (kilotons), respectively, representing the entire bay which was in a slight state of sediment loss under the typhoon

during P1 (Case 1), with an amount of 0.23 kt. Meanwhile, the transport of suspended sediments inside the bay across transect E3 was eastward, with an amount of 3.31 kt.

When the typhoon approached the domain (P2), Lingding Bay was affected by the stronger southeasterly wind instead of the northeasterly wind in P1; thus, the mean northwestward current forced a large number of suspended sediments to move landward in the bay (Fig. 19b). In Case 1, suspended sediments were imported from both the west and east sides of Point A across transect E1 during P2, with an amount of 237.99 kt. Likewise, the number of suspended sediments imported across transect E2 also increased by approximately 50 kt. However, a quarter of those imported sediments were exported landward across transects E4 and E5 into upstream outlets caused by strong winds. Consequently, the sediment budgets in the west and east sides of the bay were +18.85 and +202.05 kt, respectively, indicating that the whole bay was in a state of sediment gain during P2 (Case 1), with an amount of 220.90 kt. Whether on the north or south side of Point B, the transport of suspended sediments inside the bay across transect E3 was eastward, with a total amount of 172.3 kt.

After the typhoon made landfall (P3), the direction of sediment transport on both the west and east sides of transect E1 changed to seaward in Case 1 (Fig. 19c). Sediments started to be exported out of the east side of Lingding Bay across transect E2, with a larger sediment transport of 78.45 kt. Suspended sediments were transported from upstream outlets across transects E4 and E5, with a total import of 59.12 kt. Consequently, the sediment budgets of the west and east sides were -206.13 and -164.27 kt, respectively, indicating that both sides of the bay were in a state of sediment loss. The total amount of sediment loss was 370.40 kt, i.e., 0.37 Mt. Note that this sediment transport was quite large under Typhoon Mangkhut relative to that under normal weather conditions (e.g., Zhang et al. (2021) found that Lingding Bay received only 8.67 Mt of sediment load from the four river outlets inside the estuary in 2009). The sediment transport inside Lingding Bay on the north side of Point B was eastward, while more sediments were transported westward across transect E3 on the south side of Point B. Therefore, the total transport of suspended sediments inside the bay was westward, with an amount of 120.36 kt.

In Case 1, during the entire typhoon from P1 to P3, the distribution pattern of sediment transport across all transects (Fig. 19d) was similar to that in P3, except for the opposite transport across transect E4. The west side of Lingding Bay was still in a state of sediment loss as in P3, with a sediment budget of -199.21 kt; however, the east side of the bay was in a state of sediment gain due to the massive contribution of imported sediment during P2, with a sediment budget of +49.48 kt. This indicates that the overall state of suspended load sediment transport in Lingding Bay was a sediment loss from P1 to P3, with an amount of 149.73 kt. Additionally, the directions of sediment transport inside the bay from P1 to P3 across transect E3 were the same as those in P3, but more sediments were transported eastward on the north side of Point B. On the whole, suspended sediments were transported eastward inside Linding Bay across transect E3, with a total amount of 55.25 kt.

Now, let us compare Case 2 (without waves) (Figs. 19e–h) with Case 1 (Figs. 19a–d). The sediment gain and loss patterns within Lingding Bay were similar in the two cases, except for the opposite transport in the shoal on the west side of Point A during P2 in Case 2 (Fig. 19f). As a result, the net sediment transport across E1 in Case 2 was also seaward, with a larger amount of 202.93 kt (Fig. 19h) than 123.70 kt in Case 1 (Fig. 19d) during the entire typhoon from P1 to P3. Generally, the magnitude of the sediment budget was larger in Case 2 than in Case 1. From P1 to P3, the magnitude of the overall sediment loss from Lingding Bay increased by about 73% in Case 2 relative to Case 1 because of the increase in sediment loss on the west side and the decrease in sediment gain on the east

side. Owing to the shallow depth of the shoals in Lingding Bay, the strong wind-induced current without waves (Case 2) was strong enough to erode the bed sediments, although more bed sediments could be eroded and re-suspended when considering the enhanced bottom shear stress induced by the waves (Case 1). As illustrated (Fig. 17), the strong wind-induced current was weakened owing to the joint effect of wave radiation stress and enhanced bottom shear stress; hence, the magnitude of the resulting sediment transport rate considering wave effects (Case 1) was smaller than that without wave effects (Case 2), especially near the west shore. When waves were included (Case 1), the extent of sediment transport between the west and east sides of Lingding Bay during all three periods was more intense than that without waves (Case 2), regardless of whether the sediment transport was eastward or westward. This illustrates that the wave-current interaction strengthened the sediment transport between the two sides of Lingding Bay under typhoon conditions.

5.2. Role of weather conditions

Here, we analyse the effects of the wave-current interaction and wind-induced current under different weather conditions. This will help us isolate unique characteristics under typhoon conditions.

5.2.1. Under extreme weather conditions

In both Cases 1 and 3, wave effects were considered (see Figs. 11a and 15b); thus, their differences show the exceptionally strong influence of the typhoon. In Case 1, the TM zone expanded southwestward from the WS of Lingding Bay along the west coast of the PRE, forming a continuous area with SSC and increasing to more than six times that in Case 3. For the surface and near-bottom layers, the influenced areas in Case 1 are 8.7 and 4.4 times larger than those in Case 3, respectively. Compared with Case 3 (Fig. 18c), the suspended sediment flux in Case 1 (Fig. 18a) showed a significant increase between 21.5°N and 22.5°N. The maximum increment of flux appeared in the ME, with a difference of 0.91 kg/(m^2·s). Overall, the influence of Typhoon Mangkhut on SSC distribution was significant.

5.2.2. Under normal weather conditions

Under normal weather conditions in Cases 3 and 4 (Figs. 15b and 15c), the averaged SSC distributions in the surface layer show that TM occurred in the WS of the PRE, with a relatively high concentration of approximately 0.10 g/L. Areas of higher concentrations were also located at the mouths of the western outlets. The average suspended sediment-affected areas in the surface and near-bottom layers in Case 3 were approximately 530 and 1,260 km^2, respectively, approximately 12 and 70 km^2 larger than those in Case 4. Considering wind wave effects, the differences in SSC and current velocity were small, and the relatively significant increases in SSC mainly occurred at the Yamen outlet and the west coast of the HE, with no evident changes occurring in the other area. Similarly, their averaged suspended sediment fluxes (Figs. 18c and 18d) showed small differences in magnitude and direction. Clearly, the wave-current interaction is not the main factor affecting sediment transport under normal weather conditions.

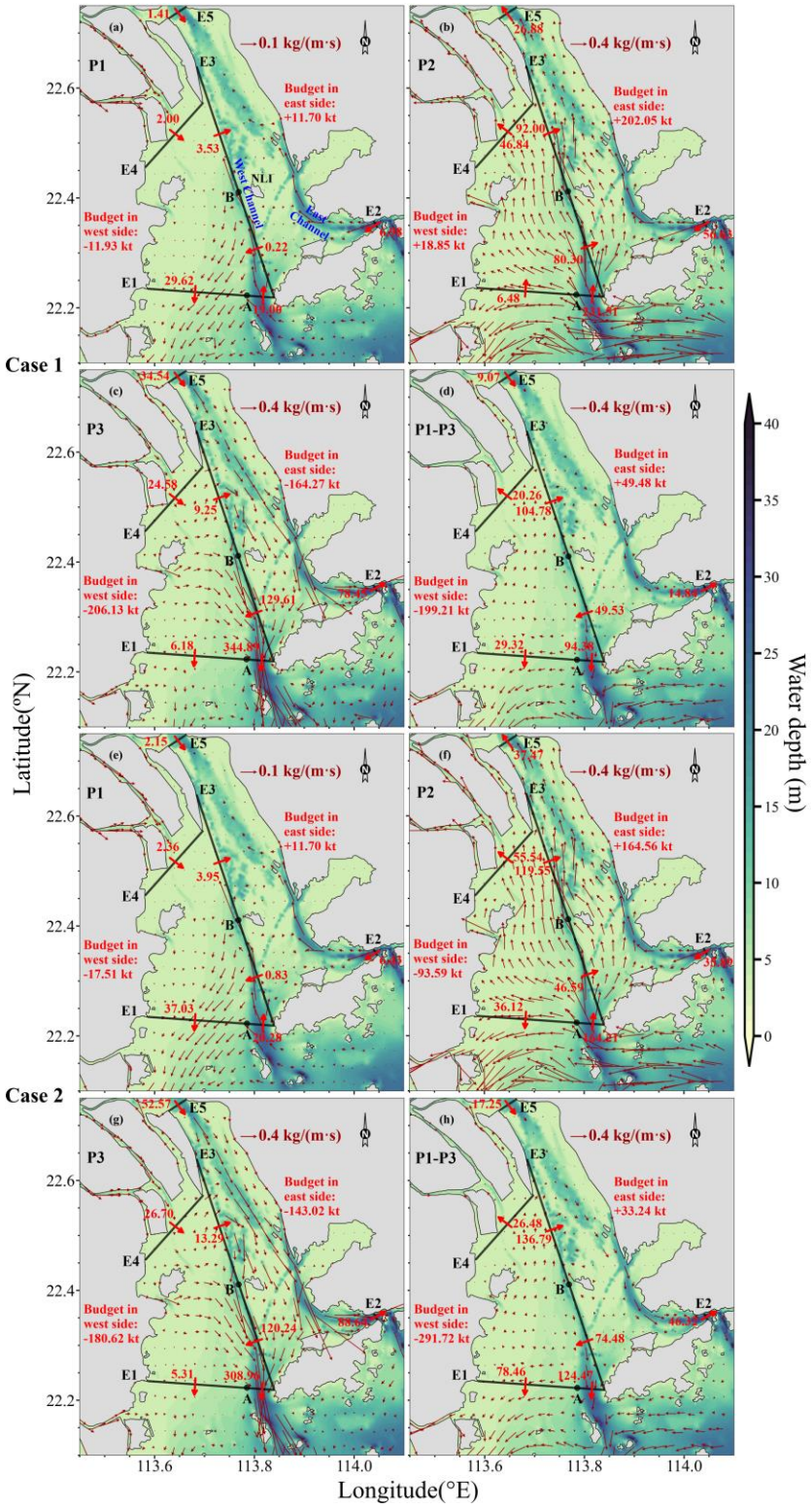

Fig. 19 Sediment budgets of Lingding Bay in Case 1 (a–c) and Case 2 (d–f) during three periods. E1–E5 are five transects; Point A, with a depth of 10 m, is located at E1, where the bathymetry gradually becomes deeper from west to east; Point B is located at E3 near Neilingding Island (NLI in (a)). The ruby red vectors are averaged distributions of depth-integrated sediment transport rate for each period (a–c and e–g) and the average of the three periods (d and h). The red arrows perpendicular to the transect represent the sediment transport across the transect over each period.

5.3. Roles of typhoon path and intensity

For an estuary facing south to the open ocean, a northwestward typhoon results in erosion. In Cases 5a and 5b, the typhoon moved along paths M1 and M2, respectively, with a southward and northward parallel shift of 0.5° from the path of Typhoon Mangkhut (Fig. 7b). Note that there were no changes in typhoon intensity for Cases 5a and 5b. The PRE suffered the greatest impact from the typhoon moving along path M2, which is closer to the PRE, while the smallest impact came from the typhoon moving along path M1 that is further from the PRE. The corresponding areas of the averaged surface SSC at a concentration greater than 0.10 g/L reached 2,527 and 7,130 km^2, respectively, in Cases 5a and 5b during P2 (Figs. 20a and 20b). As a result, the increase in the area in Case 5b is 53.9% of that in Case 1, while the decrease in the area in Case 5a is 45.5% of that in Case 1.

In Case 6a (or Case 6b), the original intensity was multiplied by a coefficient for the whole domain based on the ratio of the averaged wind speed between Case 5a (or Case 5b) and Case 1, varying with each computational grid. As a result, Cases 6a and 6b maintained the mean impact intensities suffered by the PRE to be the same as Cases 5a and 5b, respectively, but with their moving paths being the same as the original path of Typhoon Mangkhut. The area of the averaged surface SSC at a concentration greater than 0.10 g/L reached 3,206 and 6,114 km^2, respectively, in Cases 6a and 6b during P2 (Figs. 20c and 20d). Accordingly, the increase in the area in Case 6b was 31.9% of that in Case 1, while the decrease in the area in Case 6a was 30.8% of that in Case 1.

In the four simulations of Cases 5a, 5b, 6a and 6b, the maximum averaged SSC occurred at the Modaomen outlet in the surface layer, at 0.32, 0.75, 0.36 and 0.65 g/L, respectively. Compared with the results of Case 1, the southeast wind field generated by typhoon path M2 is more consistent with the orientation of the PRE than that of the original path and typhoon path M1. The results of Cases 5 and 6 show that, under the same typhoon intensity, the erosion degree is closely related to the relative location of the estuary and typhoon.

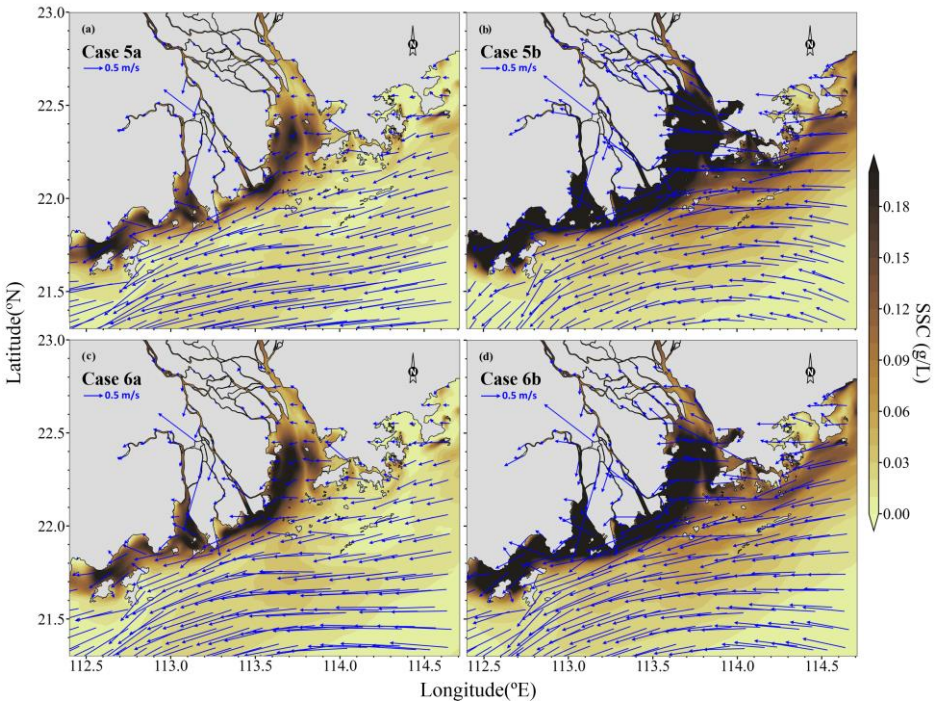

Fig. 20 Averaged SSC and currents of Cases 5 and 6 in the surface layer during P2.

6. Conclusions

To study suspended sediment transport in the PRE during Typhoon Mangkhut in 2018, we set up a 3D numerical model of SCHISM-WWM-SED-3D, which uses an unstructured grid and couples tide-wave-sediment model components. The results are validated using in situ data measured in the PRE in August 2007. The sediments in the model consist of two particle sizes. The model skills show good performance in reproducing sediment transport during Typhoon Mangkhut. Because it is difficult to collect data during a typhoon, the feasibility of a coupled model reproducing the distribution of SSC under typhoon conditions is verified and confirmed using the ocean colour data derived after Typhoon Mangkhut passed the study area.

The surface current and SWH fields respond directly to the movement of the typhoon, showing obvious cyclone features in their distribution. Owing to the topography and to Typhoon Mangkhut's path, the near-bottom wave orbital velocity increases mainly at the western outlets, and the distribution of bottom shear stress has an obvious increase in area coverage, which is between the western outlets and the 30-m isobath. In the area where water is shallower than 20 m, the increased total suspended sediment concentration is dominated by the regional erosion of fine sediment, which is caused by near-bottom wave orbital velocity and bottom shear stress, especially in the ME and HE and along the entire west coast. For the deeper coastal zone, at depths between 20 and 30 m offshore of the western coast, the high total suspended sediment concentrations contribute to fine sediment transport from the upper and middle estuaries by southwestward advection. A small amount of sand is eroded and moved locally because of the corresponding incremental distribution of the bottom shear stress. The variation in SSC has a time lag compared with the variation of other dynamic fields during the typhoon, resulting in a maximal SSC 1 h after the typhoon landfall. The horizontal distribution characteristics of the SSC are similar for all vertical layers.

According to the sensitivity experiments, the SSC values associated with wave-current interaction are much higher due to wave-enhanced bottom shear stress in the surface and near-bottom layers, achieving 1.5 and 1.3 times greater, respectively, which is larger than those simulated without the waves under the same typhoon conditions. The ME is the most affected area of the SSC during the typhoon when wave effects are included in the model. This clearly indicates that the wave effects on the increased sediments are quite important during typhoons. Meanwhile, the westward currents in all layers obviously decrease owing to the joint effect of the wave radiation stress and enhanced bottom shear stress. When the sediments moved westward under the forcing by Typhoon Mangkhut, wave-induced currents play the main role in reducing the suspended sediment export to the west; thus, a relatively high concentration area is generated along the 20-m isobath in the ME. During approach (P1), landfall (P2) and retreat (P3) of Typhoon Mangkhut, Lingding Bay experienced two transitions in sediment budgets. First, it changed from a slight state of sediment loss to a relatively high state of sediment gain, and then changed into an even greater state of sediment loss in P3. During an M_2 tidal cycle after Typhoon Mangkhut made landfall (P3), the net seaward suspended load sediment transport across Lingding Bay reached 0.37 Mt, which is roughly one twenty-third of the annual riverine load received in the bay. During the entire typhoon, covering three M_2 tidal cycles (P1-P3), the overall state of suspended load sediment transport in Lingding Bay was sediment loss, with the magnitude of sediment loss on the west side being larger than that of sediment gain on the east side. The magnitude of the overall sediment loss in Lingding Bay would be enlarged unrealistically by approximately 73% if the wave effects are excluded. In each period, the extent of sediment transport between the two sides

of the bay is strengthened by the wave-current interaction under typhoon conditions. Moreover, we determine that the net effect of wave-current interaction and strong wind-induced current under typhoon conditions is essential for erosion, which resulted in the SSC-influenced areas under Typhoon Mangkhut being about 8.7 and 4.4 times as large as those under normal weather for the surface and near-bottom layers, respectively. These effects are relatively weak under normal weather conditions. The TM moves from the WS of Lingding Bay under normal weather to the ME along the path of the typhoon. For a typhoon with the intensity of Typhoon Mangkhut, the relative location of the typhoon path with respect to the estuary has a more significant effect on erosion than the intensity of the typhoon. In future work, we plan to obtain more field data under strong typhoon conditions with the help of advanced observation methods, and then use these field data together with a more comprehensive integrated model system to further study sediment transport processes in the PRE under extreme weather events.

Acknowledgements

This study was supported by the National Key R&D Program of China (2019YFB1600700), the Science, Technology and Innovation Commission of Shenzhen Municipality (JCYJ20210324105401004), the National Nature Science Foundation of China (41830540, U20A20104 and 42076216), the Innovation Group Project of Southern Marine Science and Engineering Guangdong Laboratory (Zhuhai) (311021004), the Project of State Key Laboratory of Satellite Ocean Environment Dynamics (SOEDZZ2003 and SOEDZZ2101) and the Oceanic Interdisciplinary Program of Shanghai Jiao Tong University (SL2020ZD204). ED is an honorary research associate with the Belgian Fund for Scientific Research (F.R.S.-FNRS). We thank Prof. Eric Wolanski for his advice during this study. We also thank the editors and two anonymous reviewers for their valuable comments and suggestions for improving this paper.

References

Ariathurai, R., Arulanandan, K., 1978. Erosion rates of cohesive soils. Journal of Hydraulic Division-ASCE 104 (2), 279–283.

Battjes, J.A., 1974. Computation of set-up, longshore currents, run-up and over-topping due to wind-generated waves. Department of Civil Engineering, Delft University of Technology.

BCRS (Bulletin of China River Sediment), 2007. Press of Ministry of Water Resources of the People's Republic of China. http://www.cjh.com.cn/.

Boudet, L., Sabatier, F., Radakovitch O., 2017. Modelling of sediment transport pattern in the mouth of the Rhone delta: Role of storm and flood events. Estuar. Coast. Shelf Sci. 198 (Part B), 568–582.

Cacchione, D.A., Drake, D.E., 1982. Measurements of storm-generated bottom stresses on the continental shelf. J. Geophys. Res 87 (C3), 1952–1960.

Carrere, L., Lyard, F., Cancet, M., Guillot, A., Picot, N., 2016. FES 2014, a new tidal model—Validation results and perspectives for improvements. In Proceedings of the ESA living planet symposium, 9–13.

Chen, X.H., Chen, Y.Q., Lai, G.Y., 2003. Modeling of the transport of suspended solids in the Estuary of Zhujiang River. Acta Oceanol. Sin. 25 (2), 120–127 (in Chinese with English abstract)

Chen, Y., Wai, O.W.H., Li, Y.S., Lu, Q.M., 1999. Three-dimensional numerical modeling of cohesive sediment transport by tidal current in Pearl River Estuary. Int. J. Sediment Res. 14 (2), 107–123.

Chen, Y.R., Chen, L.H., Zhang, H., Gong, W.P., 2019. Effects of wave-current interaction on the Pearl River Estuary during Typhoon Hato. Estuar. Coast. Shelf Sci. 228, 106364.

Dai, S.B., Yang, S.L., Cai, A.M., 2008. Impacts of dams on the sediment flux of the Pearl River, southern China. Catena. 76 (1), 36–43.

Ding, P.X., Hu, K.L., Kong, Y.Z., Zhu, S.X., 2003. Numerical simulation of total sediment under waves and currents in the Changjiang Estuary. Acta Oceanol. Sin. 25 (5), 113–124.

Dong, L.X., Su, J.L., Li, Y., Xia, X.M., Guan, W.B., 2006. Physical Processes and Sediment Dynamics in the Pearl River. In: Wolanski E. (eds) The Environment in Asia Pacific Harbours. Springer, Dordrecht. https://doi.org/10.1007/1-4020-3655-8_9

Dukhovskoy, D.S., Morey, S.L., O'Brien, J.J., Martin, P.J., Cooper, C., 2009. Application of a vanishing quasi-sigma vertical coordinate for simulation of high-speed deep currents over the Sigsbee Escarpment in the Gulf of Mexico. Ocean Model. 28 (4), 250–265.

Gan, J., Li, L., Wang, D.X., Guo, X.G., 2009. Interaction of a river plume with coastal upwelling in the northeastern South China Sea. Cont. Shelf Res. 29, 728–740.

Grant, W., Madsen, O., 1982. Movable bed roughness in unsteady oscillatory flow, J. Geophys. Res., 87(C1), 469–481.

Green, M.O., Vincent, C.E., McCave, I.N., Dickson, R.R., Rees, J.M., Pearson, N.D., 1995. Storm sediment transport: observations from the British North Sea shelf. Cont. Shelf Res. 15 (8), 889–912.

Guan, W.B., Wong, L.A., Xu, D.F., 2003. Modeling nitrogen and phosphorus cycles and dissolved oxygen in the Zhujiang River Estuary. Part I . Model development. Acta Oceanol. Sin. 25(1), 52–56 (in Chinese with English abstract).

Hsu, T.W., Liau, J.M., Zanke, U., Roland, A., Mewis, P., 2005. Development and implement of a spectral finite element wave model. In: Edge, B. (Ed.), Proceedings of the Fifth International

Symposium on Wave Measurement and Analysis, Madrid.

Hu, J.T., Li, S.Y., 2009. Simulation of water and suspended sediment fluxes in Pearl River Delta during summer season. J. Hydraul. Eng. 40 (11), 1290–1298 (in Chinese with English abstract).

Hu, J.T., Li, S.Y., Geng, B.X., 2011. Modeling the mass flux budgets of water and suspended sediments for the river network and estuary in the Pearl River Delta, China. J. Mar. Syst. 88 (2), 252–266.

Jerlov, N.G., 1976. Marine Optics, Elsevier, New York.

Liu, G.P., Cai, S.Q., 2019. Modeling of suspended sediment by coupled wave-current model in the Zhujiang (Pearl) River Estuary. Acta Oceanol. Sin. 38 (7), 22–35.

Liu, L.S., Lv, X.Y., Gao, S.Z., 2019. Overview of typhoon activities over western North Pacific and the South China Sea. Journal of Marine Meteorology 39 (2), 1–12 (in Chinese with English abstract).

Liu, R.Q., Wang, Y.P., Gao, J.H., Wu, Z.Y., Guan, W.B., 2016. Turbidity maximum formation and its seasonal variations in the Zhujiang (Pearl River) Estuary, southern China. Acta Oceanol. Sin. 35 (8), 22–31.

Liu, X.H., Huang, W.R., 2009. Modeling sediment resuspension and transport induced by storm wind in Apalachicola Bay, USA. Environ. Modell. Softw. 24 (11), 1302–1313.

Longuet-Higgins, M. S., Stewart, R.W., 1964. Radiation stresses in water waves; a physical discussion, with applications. Deep Sea Res. Oceanogr. Abstr. 11(4), 529–562, https://doi.org/10.1016/0011-7471(64)90001-4

Miller, R.L., McKee, B.A., 2004. Using MODIS Terra 250 m imagery to map concentrations of total suspended matter in coastal waters. Remote Sens. Environ. 93 (1–2), 259–266.

Morton, R.A., Gibeaut, J.C., Paine, J.G., 1995. Meso-scale transfer of sand during and after storms: implications for prediction of shoreline movement. Mar. Geol. 126 (1995), 161–179.

Ni, P.T., Wei, X., Wu, C.Y., Liu, H., 2011. Tidal energy flux and dissipation in the Pearl River Estuary. The Ocean Engineering 29 (3), 67–75 (in Chinese with English abstract).

Nurser, A.J.G., Marsh, R., Williams, R.G., 1999. Diagnosing water mass formation from air-sea fluxes and surface mixing. J. Phys. Oceanogr. 29 (7), 1468–1487.

Pang, H.L., Gao, H.W., Song, P.P., You, D.W., Chen, J., 2006. Analysis of diffuse route of the Zhujiang River diluted water in summer. Marine Forecasts 23 (3), 58–63 (in Chinese with English abstract).

Pinto, L., Fortunato, A.B., Zhang, Y., Oliveira, A., Sancho F.E.P., 2012. Development and validation of a three-dimensional morphodynamic modelling system for non-cohesive sediments. Ocean Model. 57–58, 1–14.

Rascle, N., Ardhuin, F., 2013. A global wave parameter database for geophysical applications. Part 2: model validation with improved source term parameterization. Ocean Model. 70 (10), 174–188.

Roland, A., 2009. Development of the WWMII (Wind Wave Model) II - spectral wave modelling on unstructured meshes. Ph.D. Thesis. Darmstadt University of Technology, Darmstadt.

Roland, A., Zhang, Y.J., Wang, H.V., Meng, Y., Teng, Y.-C., Maderich, V., Brovchenko, I., Dutour-Sikiric, M., Zanke, U., 2012. A fully coupled 3D wave-current interaction model on unstructured grids. J. Geophys. Res.: Oceans (1978–2012) 117 (C11), 1–18.

Shen, H.T., He, S.L., Mao Z.C., Li, J.F., 2001. On the turbidity maximum in the Chinese estuaries. Journal of Sediment Research (1), 23–29 (in Chinese with English abstract).

Soulsby, R.L., 1997. Dynamics of marine sands: a manual for practical applications. Thomas Telford,

H.R. Wallingford, England.

Soulsby, R.L., Whitehouse, R.J.S.W., 1997. Threshold of sediment motion in coastal environments. In: Stive, M.J.F. et al. (Eds.), Proceedings of the Pacific Coasts and Ports'97 conference. University of Canterbury, Christchurch, New Zealand, pp. 149–154.

Tian, X.P., 1986. A study on turbidity maximum in Lingdingyang Estuary of the Pearl River. Tropic Oceanology 5 (1), 27–35 (in Chinese with English abstract).

Umlauf, L., Burchard, H., 2003. A generic length-scale equation for geophysical turbulence models. J. Mar. Res. 61 (2), 235–265.

Wai, O.W.H., Wang, C.H., Li, Y.S., Li, X.D., 2004. The formation mechanisms of turbidity maximum in the Pearl River estuary, China. Marine Pollution Bulletin 48, 441–448.

Wang, G.F., Cao, W.X., Yang, D.T., Xu, D.Z., 2008. Variation in downwelling diffuse attenuation coefficient in the northern South China Sea. Chin. J. Oceanol. Limnol. 26 (3), 323–333.

Wang, C.H., Wai, O.W.H., Li Y.S., 2001. Two-dimensional characteristics of hydrodynamics and sediment transport in the Pearl River Estuary. Proceedings of the 29th IAHR Congress Beijing: International Association for Hydro-Environment Engineering and Research, China 2, 396–401.

Wang, C.H., Wai, O.W.H., 2006. Three-dimensional modelling of sediment transport in the Pearl River Estuary. Journal of China Institute of Water Resources and Hydropower Research 4 (4), 246–252 (in Chinese with English abstract).

Wang, T.M., Wen, Z.P., Li, Y., Liang, B.Q., Tang, X.C., 2003. Comparative Analysis of the Duration Reason of Tropical Cyclones Landfall on Guangdong. Acta Sci. Nat. Univ. Sunyatseni 42 (5), 97–100 (in Chinese with English abstract).

Warner, J.C., Butman, B., Dalyander, P.S., 2008. Storm-driven sediment transport in Massachusetts Bay. Cont. Shelf Res. 28 (2), 257–282.

Williams, J.J., Rose, C.P., 2001. Measured and predicted rates of sediment transport in storm conditions. Mar. Geol. 179(2001), 121–133.

Willmott, C. J., 1981. On the validation of models. Phys. Geogr., 2, 184–194, https://doi.org/10.1080/02723646.1981.10642213

Wong, L.A., Chen, J.C., Xue, H.J., Dong, L.X., Guan, W.B., Su, J.L., 2003. A model study of the circulation in the Pearl River Estuary (PRE) and its adjacent coastal waters: 2. Sensitivity experiments. J. Geophys. Res 108 (C5), 3157, https://doi.org/10.1029/2002JC001452

Wong, L.A., Chen, J.C., Dong, L.X., 2004. A model of the plume front of the Pearl River Estuary, China and adjacent coastal waters in the winter dry season. Cont. Shelf Res. 24, 1779–1795.

Xia, Z., Ma, S.Z., Liang, K., Shi, Y.H., 2008. The characteristics analysis of sea bottom deposit in Lingdingyang Bay of the Pearl River Estuary. Marine Geology & Quaternary Geology. 28 (2), 7–13 (in Chinese with English abstract).

Yang, H., Xie, Q.C., Li B.G., Xia, X.M., 2005. Study on the conditions of rapid siltation in deep trough in the bay. Acta Oceanol. Sin. 27 (4), 95–101 (in Chinese with English abstract).

Yang, J., Li, L.L., Zhao, K.F., Wang, P.T., Wang, D., Sou., I.M., Yang, Z.T., Hu, J., Tang, X.C., Mok, K.M., Liu, P.L-F., 2019. A comparative study of Typhoon Hato (2017) and Typhoon Mangkhut (2018)—Their impacts on coastal inundation in Macau. J. Geophys. Res: Oceans, 124 (12), 9590–9619. https://doi.org/10.1029/2019JC015249

Zhang, G., Cheng, W.C., Chen, L.H., Zhang, H., Gong, W.P., 2019. Transport of riverine sediment from different outlets in the Pearl River Estuary during the wet season. Mar. Geol. 415, 105957.

Zhang, G., Chen, Y.R., Cheng, W.C., Zhang, H., Gong, W.P., 2021. Wave Effects on Sediment

Transport and Entrapment in a Channel-Shoal estuary: The Pearl River Estuary in the Dry Winter Season. J. Geophys. Res: Oceans, 126 (4), e2020JC016905. https://doi.org/10.1029/2020JC016905

Zhang, H., Madsen, O.S., Sannasiraj, S.A., Chan, E.S., 2004. Hydrodynamic model with wave-current interaction in coastal regions. Estuar. Coast. Shelf Sci. 61 (2), 317–324.

Zhang, H.S., Ni, P.T., Wu, C.Y., 2000. 2-Dimensional Numerical Model for Estuarine Turbidity Maximum Zone. Pearl River 6, 10–12 (in Chinese with English abstract).

Zhang, Y., Swift, D.J.P., Fan, S.J., Niedoroda, A.W., Reed, C.W., 1999. Two-dimensional numerical modeling of storm deposition on the northern California shelf. Mar. Geol. 154 (1–4), 155–167.

Zhang, Y., Xia, Y.H., Qian, L.B., Zhu, P.L., 2011. Analysis on hydrological characteristics off the Pearl River Estuary in summer and winter of 2006. Journal of Tropical Oceanography. 30 (1): 20–28 (in Chinese with English abstract).

Zhang, Y.J., Ateljevich, E., Yu, H.C., Wu, C.H., Yu, J.C.S., 2015. A new vertical coordinate system for a 3D unstructured-grid model. Ocean Model. 85, 16–31.

Zhang, Y.J., Ye, F., Stanev, E.V., Grashorn, S., 2016. Seamless cross-scale modeling with SCHISM. Ocean Model. 102, 64–81.

Zhang, Y.L., Baptista, A.M., 2008. SELFE: a semi-implicit Eulerian-Lagrangian finite-element model for cross-scale ocean circulation. Ocean Model. 21, 71–96.

Zhao, Q., 2007. SWAN/ECOMSED-based three-dimensional numerical model for fine sediment transport in storm event in Huanghua Port. Journal of Sediment Research 4, 17–26 (in Chinese with English abstract).

Zhu, Z.N., Wang, H.Q., Guan, W.B., Cao, Z.Y., 2013. 3D numerical study on cohesive sediment dynamics of the Pearl River Estuary in the wet season. Journal of Marine Sciences 31 (3), 25–35 (in Chinese with English abstract).